Pulsatile pressure driven rarefied gas flow in long rectangular ducts

A Tsimpoukis, D. Valougeorgis

Pulsatile pressure driven rarefied gas flow in long rectangular ducts

Alexandros Tsimpoukis and Dimitris Valougeorgis[1]

Laboratory of Transport Phenomena, Department of Mechanical Engineering
University of Thessaly, Pedion Areos, 38334 Volos, Greece

Abstract

The pulsatile pressure driven fully-developed flow of a rarefied gas through an orthogonal duct is investigated, based on the time-dependent linear BGK equation, by decomposing the flow into its steady and oscillatory parts. The investigation is focused on the oscillatory part, which is characterized by the gas rarefaction and oscillation parameters, the duct aspect ratio and the accommodation coefficient. As the oscillation frequency is increased the amplitude of all macroscopic quantities is decreased, while their phase angle lag is increased reaching the limiting value of $\pi/2$. As the gas becomes more rarefied higher frequencies are needed to trigger this behavior. At small and moderate frequencies there is a critical degree of gas rarefaction, where a maximum flow rate is obtained. As the duct aspect ratio is decreased and tends to zero, the flow rate and mean wall shear stress amplitudes are increased, while their phase angle lags are slightly affected. The accommodation coefficient has a significant effect on the amplitude and a very weak one on the phase angle of the macroscopic quantities. The computation of the inertia and viscous forces clarifies when the flow consists of only one oscillating viscous region or of two regions, namely the inviscid piston flow in the core and the oscillating Stokes layer at the wall with the velocity overshooting. Finally, the time average oscillatory pumping power is increased as the oscillation frequency is reduced and its maximum value is one half of the corresponding steady one.

[1] Corresponding author: diva@mie.uth.gr

1. Introduction

In the hydrodynamic (or viscous) regime, pulsatile and oscillatory pressure-driven fully-developed flows, through channels of various cross sections have received, over the years, considerable attention [1-12]. Superimposing the oscillatory flow and the corresponding steady-state flow yields the pulsatile pressure driven flow [4]. Mathematical treatment of pulsatile flows in various geometries includes Fourier expansion [5], Laplace transform [6] and Green functions [7]. An early survey of the implemented analytical and semi-analytical methodologies may be found in [8]. It has been observed that in high frequencies, the flow lags the pressure gradient approximately by 90^o and consists of the inviscid piston flow in the core and the frictional Stokes wall layer with the velocity overshooting (the so-called Richardson effect). Pulsatile and oscillatory flows, mainly due to their technological interest (e.g. flow propagation and control, reducing fouling, promoting mixing, heat and mass exchange, photonics and electronics cooling, aero-acoustics and thermo-acoustics) remain an active area of research [9-12].

In the slip, transition and free molecular regimes however, where in addition to the oscillation frequency, the level of gas rarefaction plays a significant role in the flow properties and patterns, the corresponding work in rarefied pulsatile gas flows is very limited. Since these flows have not been investigated so far, there is both theoretical and technological interest. Following the theoretical understanding of the involved flow parameters on the macroscopic quantities in all flow regimes, rarefied pulsatile flows may be introduced in numerous microfluidics and vacuum technology applications [13-16]. In the slip regime, the oscillatory flow in rectangular channels has been solved in [17], based on the unsteady Stokes equation subject to slip boundary conditions. Of course, continuum-based models are valid provided that both the mean free path and time are much smaller than the characteristic channel size and the pressure gradient oscillation time respectively. Therefore, in the transition and free molecular regimes the flow must be modeled by kinetic theory based on the Boltzmann equation [18] or reliable kinetic model equations [19-21].

In this framework, very recently, the rarefied oscillatory flow in a cylindrical tube has been simulated, based on the linearized BGK equation, with the assumption of small oscillatory pressure gradient amplitude [22]. The velocity distributions and the flow rates have been computed in the whole range of gas rarefaction and oscillation frequency. As far

as the authors are aware of there are no other works concerning oscillatory and pulsatile pressure driven flows via kinetic modeling. Here, the analysis in [22] is extended to pulsatile flows in channels of rectangular cross section. Computational results are provided for the velocities and flow rates, as well as for the mean wall shear stress, the acting viscous and inertia forces and the pulsatile pumping power.

It is worthwhile to note that although rarefied flows due to pulsatile or oscillatory pressure gradients have received very little attention, the corresponding flows due to oscillating boundaries have been investigated in one and two dimensional configurations in a considerable number of works [23-33]. These flows are present in a variety of micro electromechanical systems, such as resonating filters, sensors and actuators [34-39], where the computation of the damping forces in the narrow gaps between moving microstructures is crucial in order to control and optimize the resolution and sensitivity of the signal. In most cases simulations are based on linearized kinetic models [19-21], which are numerically solved in an efficient and accurate manner [40].

The experience gained from the analysis and computations described in oscillatory boundary driven flows, as well as from [22], has been a great asset in the present work, where, as pointed out above, the time-dependent rarefied gas flow through a long channel of rectangular cross section driven by a pulsatile pressure gradient is solved. The remaining of the paper is organized as follows: In Section 2, all macroscopic quantities of the rarefied pulsatile gas flow are described in detail, decomposing the flow into the oscillatory and steady parts. Also, the dimensionless parameters characterizing the flow are specified. In Section 3, the kinetic equations with the associated boundary conditions and the implemented numerical scheme are provided. The numerical results are presented in Section 4 and they include the amplitude, phase angle and time evolution of the most important macroscopic quantities in terms of the parameters specifying the flow. The velocities and flow rates are given in Section 4.1, the mean wall shear stresses and the acting forces in Section 4.2 and the pumping powers in Section 4.3. The concluding remarks are outlined in Section 5. Finally, in Appendices A and B, the kinetic formulation of pulsatile flow between parallel plates and closed form expressions in the hydrodynamic and slip regimes are provided respectively.

2. Flow configuration and definition of macroscopic quantities

Consider the time-dependent isothermal flow of a monatomic rarefied gas through a long duct with a constant rectangular cross section restricted as $-H/2 \le y' \le H/2$ and $-W/2 \le x' \le W/2$. Without loss of generality, the height is assumed to be smaller or equal to the width of the channel $\left(H \le W\right)$. The area and the perimeter of the channel cross section are defined by $A' = H \times W$ and $\Gamma' = 2\left(H + W\right)$ respectively. The flow is caused by a pulsatile pressure gradient that consists of a constant part that does not vary in time and that produces a steady flow forward, plus an oscillatory part, with the oscillation frequency ω, that moves the fluid only back and forth and that produces zero net flow over each cycle. Furthermore, the duct is considered as adequately long, in order to ignore end effects and assume pulsatile fully-developed flow. This flow set-up has been extensively investigated in the hydrodynamic regime [4], while the corresponding work in the transition and free molecular regimes is limited [22].

Next, the main flow quantities of the pulsatile flow are introduced first in dimensional and then, in dimensionless form. The local pulsatile pressure gradient depends on the flow direction z' and time t'. It may be written as

$$\frac{d\hat{P}_{PUL}\left(t',z'\right)}{dz'} = \frac{dP_S\left(z'\right)}{dz'} + \frac{d\hat{P}\left(z',t'\right)}{dz'} = \frac{dP_S\left(z'\right)}{dz'} + \frac{dP\left(z'\right)}{dz'}\cos\left(\omega t'\right) =$$

$$= \frac{dP_S\left(z'\right)}{dz'} + \frac{dP\left(z'\right)}{dz'}\Re\left[\exp\left(-i\omega t'\right)\right] \qquad (1)$$

where $d\hat{P}_{PUL}/dz'$, dP_S/dz' and $d\hat{P}/dz'$ refer to the pulsatile, steady and oscillatory pressure gradients, $dP\left(z'\right)/dz'$ is the amplitude of the oscillating pressure gradient, while $\Re$ denotes the real part of a complex expression, with $i = \sqrt{-1}$. It is evident that the time average over one period of the pressure gradient of the oscillatory flow is zero, while of the pulsatile flow is different than zero and equal to the steady pressure gradient. Due to the linearity of Eq. (1), the steady and oscillatory parts of the pulsatile fully-developed flow can be solved independently of each other. This is a useful breakdown, because the steady part of the flow has already been solved in [41,42] and therefore, only the oscillatory part remains for investigation.

The pulsatile pressure gradient generates a gas flow in the $z'-$direction, which is characterized by its pulsatile velocity and shear stress distributions given by

$$\hat{U}_{PUL}\left(t',x',y'\right)=U_S\left(x',y'\right)+\hat{U}\left(t',x',y'\right)=U_S\left(x',y'\right)+\Re\left[U\left(x',y'\right)\exp\left(-i\omega t'\right)\right] \quad (2)$$

and

$$\hat{\Pi}_{PUL,jz'}\left(t',x',y'\right)=\Pi_{S,jz'}\left(x',y'\right)+\hat{\Pi}_{jz'}\left(t',x',y'\right)=$$

$$=\Pi_{S,jz'}\left(x',y'\right)+\Re\left[\Pi_{jz'}\left(x',y'\right)\exp\left(-i\omega t'\right)\right],\quad j=x',y' \quad (3)$$

respectively. In all cases the pulsatile quantities consist of the steady and oscillatory parts. The superscript ^ always denotes time-dependent quantities. The complex functions $U\left(x',y'\right)$, $\Pi_{x'z'}\left(x',y'\right)$ and $\Pi_{y'z'}\left(x',y'\right)$ completely determine the oscillatory pressure driven flow. From Eqs. (1-3), it is seen that in general, the pressure gradient, the velocity and the shear stress are not in phase with each other. Integrating the velocity over the cross section and the wall shear stress along the perimeter of the cross section the mean velocity and mean wall shear stress are defined:

$$\bar{\hat{U}}_{PUL}\left(t'\right)=\frac{1}{A'}\iint_{A'}\hat{U}_{PUL}\left(t',x',y'\right)dA'=\bar{U}_S+\bar{\hat{U}}\left(t'\right)=\bar{U}_S+\Re\left[\bar{U}\exp\left(-i\omega t'\right)\right] \quad (4)$$

$$\bar{\hat{\Pi}}_{PUL,W}\left(t'\right)=\int_{\Gamma'}\hat{\Pi}_{PUL,jz}\left(t',x',y'\right)d\Gamma'=\bar{\Pi}_{S,W}+\bar{\hat{\Pi}}_W\left(t'\right)=\bar{\Pi}_{S,W}+\Re\left[\bar{\Pi}_W\exp\left(-i\omega t'\right)\right] \quad (5)$$

The quantities with the subscript "S" always denote the steady part, while $\bar{U}$ and $\bar{\Pi}_W$ are complex and related to the oscillatory part.

Furthermore, the pulsatile mass flow rate is defined as

$$\hat{\dot{M}}_{PUL}\left(t'\right)=\iint_{A'}\rho\left(t',z'\right)\hat{U}_{PUL}\left(t',x',y'\right)dA'=\dot{M}_S+\dot{M}\left(t'\right)=\dot{M}_S+\Re\left[\dot{M}\exp\left(-i\omega t'\right)\right] \quad (6)$$

where $\dot{M}_S$ and $\dot{M}\left(t'\right)$ denote the steady and oscillatory mass flow rates, while the mass density $\rho=\rho\left(t',z'\right)$ varies in time and in the axial direction (it is constant at each cross section) and it is defined by the equation of state once the operating pressure and temperature are specified. The net oscillatory mass flow rate over one oscillation cycle is zero.

Next, based on the mean velocity and wall shear stress, the inertia (or acceleration) $\hat{F}_I'\left(t'\right)$ and viscous $\hat{F}_V'\left(t'\right)$ forces acting on a fluid volume $A'dz'$ passing through the channel are given by

$$\hat{F}'_{PUL,I}\left(t'\right)=\rho dz'A'\frac{\partial\bar{\hat{U}}_{PUL}\left(t'\right)}{\partial t'}=\rho dz'A'\frac{\partial\bar{\hat{U}}\left(t'\right)}{\partial t'}=\hat{F}'_{I}\left(t'\right) \tag{7}$$

and

$$\hat{F}'_{PUL,V}\left(t'\right)=F'_{S,V}+\hat{F}'_{V}\left(t'\right)=dz'\Gamma'\left(\bar{\Pi}_{S,W}+\bar{\hat{\Pi}}_{W}\left(t'\right)\right). \tag{8}$$

As expected the inertia force is related only to the oscillatory part, while the viscous force has both steady and oscillatory parts. At any point in time, the driving pressure force

$$\hat{F}'_{PUL,P}\left(t'\right)=F'_{S,P}+\hat{F}'_{P}\left(t'\right)=A'dP_{S}+A'd\hat{P}\left(t'\right) \tag{9}$$

must equal the net sum of the viscous and inertia forces that may add or subtract from each other at different times within the oscillatory cycle. Then, the following steady and oscillatory force balances are formed:

Steady: $A'dP_{S}=dz'\Gamma'\bar{\Pi}_{S,W}$ (10)

Oscillatory: $A'd\hat{P}\left(t'\right)=\rho dz'A'\frac{\partial\bar{\hat{U}}\left(t'\right)}{\partial t'}+dz'\Gamma'\bar{\hat{\Pi}}_{W}\left(t'\right)$ (11)

It is noted that due to the fully-developed flow there is no net momentum flux.

Finally, the pumping power needed to drive the pulsatile flow is defined as

$$\hat{E}'_{PUL}\left(t'\right)=E'_{S}+\hat{E}'\left(t'\right) \tag{12}$$

where the steady the oscillatory pumping powers are given by the product of the corresponding acting pressure forces times the mean velocities written as

$$E'_{S}=A'dP_{S}\bar{U}_{S} \tag{13}$$

and

$$\hat{E}'\left(t'\right)=A'd\hat{P}\left(t'\right)\bar{U}\left(t'\right)=A'dP\cos\left(\omega t'\right)\Re\left[\bar{U}\exp\left(-i\omega t'\right)\right] \tag{14}$$

respectively. Since the oscillatory part $\hat{E}'\left(t'\right)$ does not produce any net flow forward and since the steady part E'_{S} is the same as that in steady flow, any power expenditure on the oscillatory part of the flow reduces the efficiency of the flow. It is noted that the integral of the oscillatory pumping power over one cycle in nonzero, hence oscillatory flow requires energy to maintain even the net flow is zero. This energy expenditure is required to balance the energy dissipation at the channel wall, while the net energy expenditure for accelerating and decelerating the flow is zero [4].

The parameters which define the problem in dimensional form include the gas properties, the operating pressure and temperature, the channel geometry and the oscillation frequency. They are significantly reduced by introducing the corresponding quantities in dimensionless form, allowing in parallel, a more detailed flow investigation.

To achieve that the two dimensionless flow parameters defining the present pulsatile flow are specified [22]. The first one is the gas rarefaction parameter δ and it is given by

$$\delta = \frac{PH}{\mu \upsilon} \tag{15}$$

where μ is the gas viscosity at some reference temperature T and $\upsilon = \sqrt{2RT}$ is the most probable molecular speed ($R = k_B / m$, with k_B denoting the Boltzmann constant and m the molecular mass, is the gas constant). The rarefaction parameter is proportional to the inverse Knudsen number. The second one is the frequency parameter θ and it is given by

$$\theta = \frac{P}{\mu \omega} \tag{16}$$

where $\left(P/\mu\right)$ is the intermolecular collision frequency and ω the oscillation frequency. Hence, small and large values of θ correspond to high and low pressure gradient oscillation respectively. As $\theta \to \infty$, the oscillatory part of the flow diminishes. The two parameters are independent of each other.

Also, the dimensionless independent space and time variables

$$x = x'/H,\ y = y'/H,\ z = z'/H \text{ and } t = t'\omega, \tag{17}$$

with $-1/2 \le y \le 1/2$ and $-H/\left(2W\right) \le x \le H/\left(2W\right)$ are introduced. The dimensionless area and perimeter of the channel cross section are defined by $A = A'/H^2$ and $\Gamma = \Gamma'/H$ respectively, while $\Gamma / A = 2\left(1 + H/W\right)$. The dimensionless amplitude of the local oscillatory pressure gradient is

$$X = \frac{H}{P\left(z'\right)} \frac{dP\left(z'\right)}{dz'} = \frac{1}{P\left(z\right)} \frac{dP\left(z\right)}{dz}, \tag{18}$$

with $X << 1$. This assumption is typical in fully-developed flows (also in steady-state setups), in order to permit the linearization of the governing kinetic equation and it is valid for any pressure difference provided that the channel is adequately long [40,41]. For comparison purposes between the oscillatory and steady flow, the amplitude of the oscillatory pressure

gradient is taken equal to the steady one ($dP/dz' = dP_S/dz'$). In this way, $X = X_S$, and the peak values of the macroscopic quantities (velocity, flow rate, shear stress, and pumping power) of the oscillatory flow can be compared with the corresponding ones of the steady flow.

All velocities (pulsatile, oscillatory and steady) are non-dimensionalized by the most probable speed υ. More specifically, Eq. (2) is divided by (υX) to yield

$$\hat{u}_{PUL}(t,x,y) = u_S(x,y) + \hat{u}(t,x,y) \tag{19}$$

where $u_S(x,y)$ is the steady flow velocity and $\hat{u}(t,x,y)$ is the oscillatory flow velocity, which may be written as

$$\hat{u}(t,x,y) = \Re\left[u(x,y)\exp(-it)\right] = \Re\left[u_A(x,y)\exp\left(i\left(u_P(x,y)-t\right)\right)\right] =$$

$$= u_A(x,y)\cos\left[t - u_P(x,y)\right] \tag{20}$$

In Eq. (20) the subscripts A and P denote the amplitude and the phase angle of the complex oscillatory velocity $u(x,y)$. The mean velocities are also non-dimensionalized by the most probable speed υ and the resulting mean steady and oscillatory velocities are denoted by $\overline{u}_S$ and $\overline{\hat{u}}(t)$ respectively.

Next, the dimensionless flow rate is defined by introducing (17), (19) and (20) along with the equation of state $P = \rho\upsilon^2/2$ into Eq. (6) to obtain $\tilde{\dot{M}}_{PUL}(t') = H^2 PX\hat{G}_{PUL}(t)/\upsilon$, where

$$\hat{G}_{PUL}(t) = G_S + \hat{G}(t). \tag{21}$$

In Eq. (21), G_S is the well-known steady flow rate given by [41]

$$G_S = 2\frac{H}{W}\int_{-1/2}^{1/2}\int_{-W/(2H)}^{W/(2H)} u_S(x,y)\,dxdy \tag{22}$$

and $\hat{G}(t)$ is the oscillatory flow rate given by

$$\hat{G}(t) = 2\frac{H}{W}\int_{-1/2}^{1/2}\int_{-W/(2H)}^{W/(2H)} \hat{u}(t,x,y)\,dxdy. \tag{23}$$

The oscillatory flow rate $\hat{G}(t)$ may be also written as

$$\hat{G}(t) = \Re\left[G\exp(-it)\right] = \Re\left[G_A\exp\left(i\left(G_P - t\right)\right)\right] = G_A\cos\left(G_P - t\right) \tag{24}$$

where the flow rate G, as well its amplitude G_A and phase angle G_P, may be computed by integrating accordingly the corresponding velocity quantities. Based on the above definitions it is readily seen that the dimensionless flow rates may be connected to the dimensionless mean velocities by the following expressions: $G_S = 2\overline{u}_S$ and $\hat{G}(t) = 2\overline{\hat{u}}(t)$.

All stresses (pulsatile $\hat{\tau}_{PUL}$, oscillatory $\hat{\tau}$ and steady τ_S) are non-dimensionalized by $(2PX)$. Here, we are interested mainly in the mean pulsatile wall shear stress $\overline{\hat{\tau}}_{PUL,W}(t)$ which consists of the steady mean wall shear stress $\overline{\tau}_{S,W}$ plus the oscillatory one $\overline{\hat{\tau}}_W(t)$ written as

$$\overline{\hat{\tau}}_W(t) = \Re\left[\overline{\tau}_W\exp(-it)\right] = \Re\left[\overline{\tau}_{W,A}\exp\left(i\left(\overline{\tau}_{W,P} - t\right)\right)\right] = \overline{\tau}_{W,A}\cos\left(t - \overline{\tau}_{W,P}\right). \tag{25}$$

In Eq. (25) the subscripts A and P denote the amplitude and the phase angle of the corresponding oscillatory complex shear stresses.

All forces in Eqs. (7-9) are divided by $\left(PX_PH^2\right)$ to yield the corresponding dimensionless ones:

$$\hat{F}_{PUL,I}(t) = \hat{F}_I(t) = dzA\frac{\delta}{\theta}\frac{d\hat{G}}{dt} = dzA\frac{\delta}{\theta}G_A\sin\left(G_P - t\right) \tag{26}$$

$$\hat{F}_{PUL,V}(t) = F_{S,V} + \hat{F}_V(t) = 2dz\Gamma\left[\overline{\tau}_{S,W} + \overline{\hat{\tau}}_W(t)\right] = 2dz\Gamma\left[\overline{\tau}_{S,W} + \overline{\tau}_{W,A}\cos\left(\overline{\tau}_{W,P} - t\right)\right] \tag{27}$$

$$\hat{F}_{PUL,P}(t) = F_{S,P} + \hat{F}_P(t) = Adz\left(1 + \cos t\right) \tag{28}$$

The balance equations of the steady $F_{S,V} = F_{S,P}$ and oscillatory $\hat{F}_I(t) + \hat{F}_V(t) = \hat{F}_P(t)$ forces in dimensionless form are:

$$\text{Steady: } \overline{\tau}_{S,W} = A/(2\Gamma) = \left[4\left(1 + \frac{H}{W}\right)\right]^{-1} \tag{29}$$

$$\text{Oscillatory: } \frac{\delta}{\theta}G_A\sin\left(G_P - t\right) + 4\left(1 + \frac{H}{W}\right)\overline{\tau}_{W,A}\cos\left(\overline{\tau}_{W,P} - t\right) = \cos t \tag{30}$$

Equation (29) has been also reported in previous works related to steady fully-developed flows through channels of various cross sections [43,44]. Equation (30) is the corresponding one for oscillatory flow. The first and second terms at the left hand side refer to the inertia and

viscous forces respectively, while the right hand side refers to the pressure forces. In Section 4.3, these forces are plotted for various values of δ and θ.

Finally, the dimensionless pumping power is derived by dividing Eqs. (12-14) by $(\upsilon X)(XP)H^2$ to find $\hat{E}_{PUL}(t) = E_S + \hat{E}(t)$, where the steady pumping power is $E_S = AdzG_S / 2$ and the oscillatory one is written as

$$\hat{E}(t) = \frac{1}{2} Adz \cos t G(t) = \frac{1}{2} Adz \cos t \cdot \left[G \exp(-it) \right] =$$

$$= \frac{1}{2} Adz \cos t \cdot \left[G_A \exp\left(i\left(G_P - t \right) \right) \right] = \frac{1}{2} AdzG_A \cos t \cos\left(G_P - t \right). \qquad (31)$$

By integrating Eq. (31) over one oscillation cycle, the average pumping power over the cycle is formed as

$$\overline{E} = \frac{1}{2\pi} \int_0^{2\pi} \hat{E}(t)\, dt = \frac{1}{4} AdzG_A \cos\left(G_P \right). \qquad (32)$$

In the low frequency regime, where $G_P \to 0$ and $G_A \cdot G_S$, it is seen that the average oscillatory pumping power is half of the corresponding steady one ($\overline{E} \cdot E_S / 2$).

The prescribed pulsatile flow is solved here in the whole range of δ and θ, which may vary from zero to infinity and for various aspect ratios $H / W \in [0,1]$. The solution is based on the kinetic modeling described in the next section. The oscillatory flow rate G, mean wall shear stress $\overline{\tau}_W$ and pumping powers $\hat{E}(t)$ and $\overline{E}$ are probably the most important quantities from a technological point of view, while the oscillatory velocity $u(x, y)$ is more important from a theoretical point of view providing an insight view of the flow characteristics. All these quantities along with their time evolution are provided in the results section.

3. Kinetic formulation and numerical scheme

For arbitrary values of the parameters δ and θ the flow must be simulated based on kinetic theory, where the main unknown is the distribution function $f = f(t', \boldsymbol{r}', \boldsymbol{\xi})$, which is a function of time t', position vector $\boldsymbol{r}' = (x', y', z')$ and molecular velocity

vector $\boldsymbol{\xi}=\left(\xi_x,\xi_y,\xi_z\right)$. The unknown distribution obeys the time-dependent nonlinear two-dimensional BGK equation [18]

$$\frac{\partial f}{\partial t'}+\xi_x\frac{\partial f}{\partial x'}+\xi_y\frac{\partial f}{\partial y'}+\xi_z\frac{\partial f}{\partial z'}=\frac{P}{\mu}\left(f^M-f\right) \tag{33}$$

where $\left(P/\mu\right)$ is the collision frequency and

$$f^M\left(t',\boldsymbol{r}',\boldsymbol{\xi}\right)=n\left(\frac{m}{2\pi kT}\right)^{3/2}\exp\left[-m\left(\boldsymbol{\xi}-\hat{\boldsymbol{U}}_{PUL}\right)^2\Big/\left(2kT\right)\right] \tag{34}$$

is the local Maxwellian distribution. Due to the assumption of isothermal fully-developed flow the temperature T is constant and the number density $n=n\left(z'\right)$ varies only in the $z'-$direction. Also, the macroscopic velocity has only the $z'-$component and it is the same with the pulsatile velocity defined in Eq. (2), i.e., $\hat{\boldsymbol{U}}_{PUL}=\left(0,0,\hat{U}_{PUL}\right)$. The pulsatile velocity and shear stress (defined in Eq. (3)) at some position z' in the flow direction may be obtained by the first and second moments of f according to

$$\hat{U}_{PUL}\left(t',x',y'\right)=\frac{1}{n}\int\xi_z\tilde{f}\left(t',\boldsymbol{r}',\boldsymbol{\xi}\right)d\boldsymbol{\xi} \tag{35}$$

and

$$\hat{\Pi}_{PUL,jz'}\left(t',x',y'\right)=m\int\xi_j\left(\xi_z-\hat{U}_{PUL}\right)f\left(t',\boldsymbol{r}',\boldsymbol{\xi}\right)d\boldsymbol{\xi}\,,\quad j=x',y' \tag{36}$$

respectively.

The condition of small local pressure gradient ($X\ll 1$) allows the linearization of Eq. (33) by representing the unknown distribution function as

$$f\left(t',\boldsymbol{r}',\boldsymbol{\xi}\right)=f_0\left[1+X\hat{h}_{PUL}\left(t,x,y,\boldsymbol{c}\right)+Xz\left(1+\exp\left(-it\right)\right)\right], \tag{37}$$

where $\boldsymbol{c}=\boldsymbol{\xi}/\upsilon$, $f_0=\dfrac{n}{\pi^{3/2}\upsilon^3}\exp\left[-c^2\right]$ is the absolute Maxwellian and $\hat{h}_{PUL}\left(t,x,y,\boldsymbol{c}\right)$ is the unknown perturbed distribution function referring to the pulsatile fully-developed flow, which may be decomposed as

$$\hat{h}_{PUL}\left(t,x,y,\boldsymbol{c}\right)=h_S\left(x,y,\boldsymbol{c}\right)+\hat{h}\left(t,x,y,\boldsymbol{c}\right) \tag{38}$$

with $\hat{h}_S(x,y,\boldsymbol{c})$ and $\hat{h}(t,x,y,\boldsymbol{c})$ referring to the steady and oscillatory parts respectively. Substituting expressions (37) and (38) into Eq. (33) and introducing the dimensionless variables, yields the following two linearized BGK kinetic model equations:

$$c_x \frac{\partial h_S}{\partial x} + c_y \frac{\partial h_S}{\partial y} + c_z = \delta\left[2c_z u_S(x,y) - h_S(x,y,\boldsymbol{c})\right] \tag{39}$$

$$\frac{\delta}{\theta}\frac{\partial \hat{h}}{\partial t} + c_x \frac{\partial \hat{h}}{\partial x} + c_y \frac{\partial \hat{h}}{\partial y} + c_z e^{-it} = \delta\left[2c_z \hat{u}(t,x,y) - \hat{h}(t,x,y,\boldsymbol{c})\right] \tag{40}$$

The first one describes the steady fully-developed flow through an orthogonal duct and it is solved in [41,42]. The second one describes the oscillatory fully-developed flow and it is the one to be solved in the present work.

Since Eq. (40) is linear, it is convenient to introduce the complex distribution function $h(x,y,\boldsymbol{c})$ so that

$$\hat{h}(t,x,y,\boldsymbol{c}) = \Re\left[h(x,y,\boldsymbol{c})\exp(-it)\right]. \tag{41}$$

Also, the molecular velocity vector $\boldsymbol{c} = (c_x, c_y, c_z)$ is transformed as $\boldsymbol{c} = (\zeta, \varphi, c_z)$, where $c_r = \zeta\cos\varphi$ and $c_\varphi = \zeta\sin\varphi$. Then, Eq. (40) is rewritten in terms of h as

$$\zeta\cos\varphi\frac{\partial h}{\partial x} + \zeta\sin\varphi\frac{\partial h}{\partial y} + h\left(\delta - \frac{\delta}{\theta}i\right) + c_z = 2\delta c_z u(x,y). \tag{42}$$

The non-dimensionalization, linearization and the molecular velocity vector transformation are also applied to the velocity and the shear stress given by Eqs. (35) and (36) to obtain:

$$u(x,y) = \frac{1}{\pi}\int_{-\infty}^{\infty}\int_0^{2\pi}\int_0^{\infty} c_z h e^{-c^2}\, d\zeta\, d\varphi\, dc_z \tag{43}$$

$$\tau_{xz}(x,y) = \frac{1}{\pi}\int_{-\infty}^{\infty}\int_0^{2\pi}\int_0^{\infty} (\zeta\cos\varphi)\, c_z h e^{-c^2}\, d\zeta\, d\varphi\, dc_z \tag{44}$$

$$\tau_{yz}(x,y) = \frac{1}{\pi}\int_{-\infty}^{\infty}\int_0^{2\pi}\int_0^{\infty} (\zeta\sin\varphi)\, c_z h e^{-c^2}\, d\zeta\, d\varphi\, dc_z. \tag{45}$$

At this stage the component c_z of the molecular velocity vector may be eliminated by applying the so-called projection procedure and introducing the reduced perturbed distribution function

$$Y\left(x,y,\zeta,\varphi\right)=\frac{1}{\pi}\int_{-\infty}^{\infty}h\left(x,y,\zeta,\varphi,c_z\right)\exp\left[-{c_z}^2\right]dc_z\,. \tag{46}$$

Equation (46) is multiplied by $c_z\exp\left(-c_z^2\right)/\sqrt{\pi}$ and the resulting equation is integrated over c_z to deduce

$$\zeta\cos\varphi\frac{\partial Y}{\partial x}+\zeta\sin\varphi\frac{\partial Y}{\partial y}+\left(\delta-i\frac{\delta}{\theta}\right)Y=\delta u-\frac{1}{2}\,. \tag{47}$$

Operating similarly on the moments of h, given by Eqs. (43-45), yields:

$$u\left(x,y\right)=\frac{1}{\pi}\int_0^{2\pi}\int_0^{\infty}Ye^{-\zeta^2}\zeta\,d\zeta\,d\varphi \tag{48}$$

$$\tau_{xz}\left(x,y\right)=\frac{1}{\pi}\int_0^{2\pi}\int_0^{\infty}\left(\zeta\cos\varphi\right)Ye^{-\zeta^2}\zeta\,d\zeta\,d\varphi \tag{49}$$

$$\tau_{yz}\left(x,y\right)=\frac{1}{\pi}\int_0^{2\pi}\int_0^{\infty}\left(\zeta\sin\varphi\right)Ye^{-\zeta^2}\zeta\,d\zeta\,d\varphi \tag{50}$$

It is noted that $Y=Y_{\mathrm{Re}}+iY_{\mathrm{Im}}$ is complex and the same applies for the velocity $u\left(x,y\right)$ and the shear stresses $\tau_{jz}\left(x,y\right)$, $j=x,y$.

Turning now to the boundary conditions it is noted that Maxwell diffuse-specular boundary conditions are used. The gas–surface interaction is modeled as [18]

$$f^{+}=\alpha f_W^M+\left(1-\alpha\right)f^{-},\qquad \boldsymbol{c}\cdot\boldsymbol{n}>0\,, \tag{51}$$

where the superscripts (+) and (−) denote distributions leaving from and arriving to the boundaries respectively, f_W^M is the Maxwellian defined by the wall conditions, $0\le\alpha\le1$ is the tangential momentum accommodation coefficient corresponding to the percentage of diffuse reflection of the gas at the wall and $\boldsymbol{n}$ is the unit vector normal to the boundaries and pointing towards the flow. Following the linearization and projection procedures as defined above it is readily deduced that at the wall boundaries

$$Y^{+}=\left(1-\alpha\right)Y^{-},\qquad \boldsymbol{c}\cdot\boldsymbol{n}>0\,. \tag{52}$$

These boundary conditions are applied at $y=\pm 1/2$ and $x=\pm H/(2W)$.

It is noted that as the aspect ratio H/W is reduced, the two-dimensional flow gradually tends to the corresponding one-dimensional flow between parallel plates. In Appendix A, the formulation of the kinetic equation with the associated conditions for the limiting case of $H/W=0$ is provided.

The kinetic formulation of the oscillatory fully-developed flow setup is properly defined by Eq. (47) with the associated moments (48-50) subject to boundary conditions (52). The numerical solution is deterministic. The discretization in the molecular velocity space is performed using the discrete velocity method. The continuum spectrum $\zeta \in [0,\infty)$ is substituted by a discrete set $\zeta_m, m=1,2...M$, which is taken to be the roots of the Legendre polynomial of order M, accordingly mapped from $[-1,1]$ to $[0,\infty)$. Also, a set of discrete angles φ_n, $n=1,2...N$ equally spaced in $[0,2\pi]$ is defined. The discretization in the physical space is based on a second order central difference scheme. The discretized equations are solved in an iterative manner and the iteration map is concluded when the criteria

$$\left|u_{\mathrm{Re},i,j}^{(k+1)}-u_{\mathrm{Re},i,j}^{(k)}\right|<\varepsilon \qquad \text{and} \qquad \left|u_{\mathrm{Im},i,j}^{(k+1)}-u_{\mathrm{Im},i,j}^{(k)}\right|<\varepsilon \tag{56}$$

is fulfilled. Here, ε is the tolerance parameter, the superscript k denotes the iteration index, $i,j=1,2...L+1$ are the nodes in the physical space, while $u_{\mathrm{Re},ij}$ and $u_{\mathrm{Im},ij}$ are the real and imaginary part of macroscopic velocity respectively at each node (i,j). This numerical scheme has been extensively applied in steady-state and time-dependent flow configurations with considerable success [43-46, 22]. The numerical parameters have been gradually refined to ensure grid independent results up to at least three significant figures.

Once the kinetic problem is solved the oscillatory complex velocity $u(x,y)=u_A(x,y)\exp\left[iu_P(x,y)\right]$ and shear stress $\tau_{jz}(x,y)=\tau_{jz,A}(x,y)\exp\left[i\tau_{jz,P}(x,y)\right]$, $j=x,y$ are computed in terms of δ, θ, H/W and α. The overall oscillatory quantities of the flow rate, the mean wall shear stress and the pumping power are deduced in a

straightforward manner, based on the expressions provided in Section 2. The pulsatile flow quantities are also readily deduced by adding the corresponding steady ones.

Closing this section it is interesting to comment on the behavior of Eq. (47) at limiting values of θ and δ. When both $\delta >> 1$ and $\theta >> 1$, the flow is in the hydrodynamic or slip regimes [22]. In these regimes analytical solutions, based on the unsteady Stokes equation with either no-slip or slip boundary conditions, have been obtained and presented in Appendix B. As $\theta \to \infty$ ($\omega \to 0$) and $\delta << \theta$ (finite values of δ), Eq. (47) is reduced to the one describing the steady fully-developed flow through a rectangular duct at the corresponding δ. In the specific case of $\delta = 0$, with $\theta > 0$, the kinetic equation for steady-state flow at the free molecular limit is recovered. At the other end, as $\theta \to 0$ ($\omega \to \infty$), Eq. (47) yields $Y \to 0$, i.e., the solution tends to vanish at very high frequencies due to fluid inertia. It is expected the behavior of Eq. (47) at the limiting conditions to be reflected in the numerical results.

4. Results and discussion

Numerical results of the time evolution, as well as of the amplitude and phase angle of the main macroscopic quantities in terms of the gas rarefaction parameter δ, the oscillation parameter θ, the duct aspect ratio H/W and the accommodation coefficient α are provided, in four subsections. Section 4.1 describes the velocity distributions in pulsatile and oscillatory flows. Sections 4.2 and 4.3 describe the overall quantities of flow rate and mean acting forces (including the mean wall shear stress) respectively. Since the corresponding steady parts are well-known results are provided only for the oscillatory parts. Finally, Section 4.4 describes the oscillatory time-dependent and average pumping powers including a comparison with the corresponding steady pumping powers.

4.1 Velocity distributions

In Fig.1 the time evolution over one cycle of the oscillatory $\hat{u}(t,0,y)$ and pulsatile $\hat{u}_{PUL}(t,0,y) = u_S(0,y) + \hat{u}(t,0,y)$ velocity distributions, given in Eqs. (19-20), are plotted with respect to $y \in [-1/2, 1/2]$ at $x = 0$ in the case of a square duct ($H/W = 1$). The plots are for $\delta = [0.1, 1, 10]$ covering a wide range of the gas rarefaction and $\theta = 0.1,\ 10$

referring to high and low frequency oscillation respectively. The evolution is shown with a time step of $\pi/2$, at $t=0$, $\pi/2$, π and $3\pi/2$. As expected, the oscillatory velocity over one cycle, takes both positive and negative values (the fluid is moved forth and back) and the time average velocity over one cycle is zero (no net flow). The effect of θ on the amplitude of the oscillatory velocity is significant. As it is seen, it is greatly reduced as θ is decreased and this behavior becomes even stronger as δ is increased (less gas rarefaction). The time evolution of the pulsatile velocity is obtained by superimposing on the oscillatory velocity the corresponding steady one, which depends only on δ. Since the steady flow is independent of θ the behavior of the pulsatile velocity with respect to θ is qualitatively the same with the oscillatory one. Consequently, at large θ (e.g., $\theta=10$), where the amplitude of the oscillatory velocity is large, the difference between the amplitude of the pulsatile velocity and the corresponding steady one is also large. On the contrary, as the oscillatory flow tends to diminish, which is happening as θ is decreased and δ is increased, the pulsatile velocity gradually tends to the steady one at the corresponding δ. This is particularly evident at $\theta=0.1$ and $\delta=10$, where $\hat{u}_{PUL}(t,0,y) \approx u_S(0,y)$. As it is outlined in Section 2, the present results are based on the assumption that the amplitude of the oscillatory pressure gradient is the same with the steady pressure gradient ($dP_S/dz' = d\hat{P}/dz'$). Having this in mind it is interesting to note that the pulsatile velocity takes only positive values, i.e., there is no flow reversal at any time. This observation may be technologically significant in applications where a pulsatile flow is desired, e.g. in order to enhance mixing or heat transfer under rarefied conditions, without however having particles moving opposite to the pumping direction or hot gas transported backwards into colder regions. In any case, if $dP_S/dz' < d\hat{P}/dz'$, although the net flow is nonzero, flow reversal may be present.

In Fig. 2, the contours of the oscillatory velocity amplitude $u_A(x,y)$ are presented in a two dimensional layout for square ($H/W=1$) and orthogonal ($H/W=0.1$) ducts, with $\delta=[0.1.1,10]$ and $\theta=0.1$. As it is seen at this relatively high oscillation frequency the effect of δ moving from the free molecular ($\delta=0.1$) through the transition ($\delta=1$) up to the slip ($\delta=10$) regime is remarkable. At $\delta=0.1$ there is a very close qualitative

resemblance with the corresponding steady one, with the velocity amplitude taking its maximum values at the center of the cross section of the duct and then, it is monotonically reduced towards the walls of the cross section. At $\delta = 10$, the situation is reversed, with the maximum amplitudes appearing in a very thin layer adjacent to the walls, while outside this layer the velocity amplitude is smaller and almost constant. At the intermediate value of $\delta = 1$ the maximum amplitudes occur in a wider region between the center and the walls of the duct. This description is valid for both aspect ratios. Furthermore, the velocity overshooting (known as the "Richardson effect"), is well-known in the hydrodynamic regime [4] and it has been also recently observed in oscillatory rarefied gas flow through a tube [22].

The oscillatory velocity amplitude u_A and phase angle u_P along the symmetry axis $x = 0$ are plotted in Figs. 3 and 4 for oscillatory flow through a square duct ($H/W = 1$) and an orthogonal duct ($H/W = 0.1$) respectively for various values of δ and θ. In the former case $x \in [-1/2, 1/2]$ and in the latter one $x \in \left[-H/(2W), H/(2W)\right]$. The objective here is to comment on the dependency of u_A and u_P on δ and θ, as well as to observe the effect of the aspect ratio H/W. Always, as θ is decreased, i.e., the oscillation frequency is increased, the amplitude u_A is reduced and the phase angle lag u_P is increased. It is also seen that in general at small δ and large θ (e.g., $\delta = 0.1$ and $\theta \geq 0.1$) the velocity amplitudes have the expected shape with their maximum appearing at the center of the duct, while the corresponding phase angles are small. However, as δ is increased and θ is reduced the velocity amplitude is flattening in the core of the flow and the maximum amplitude is appearing in a region far from the center of the orthogonal duct. At large δ and small θ (e.g., $\delta = 10$ and $\theta \leq 1$) u_A remains constant from the center of the duct until close to the wall and then, in a thin layer adjacent to the wall it is rapidly increased and decreased. The corresponding phase angle lags u_P are large, even up to $\pi/2$ with regard to the pressure gradient and they remain constant from the center of the duct until the wall layer, where they change significantly in an oscillatory manner. The thickness of the region where the velocity overshooting occurs is decreased as δ is increased and θ is reduced. Therefore, in high or even moderate frequencies (it depends also on δ), the flow consists of two layers: the inviscid piston flow in the core,

dominated by inertia forces and the frictional Stokes wall layer dominated by viscous forces. Comparing the corresponding results in Figs. 3 and 4, it is clearly seen that the velocity overshooting (or Richardson effect) appears first in the orthogonal duct and then in the square duct. For example at $\delta = \theta = 0.1$, $\delta = \theta = 1$ and $\delta = \theta = 10$, the velocity amplitudes for $H/W = 1$ (Fig. 3) take their maximum values at the duct center, while for $H/W = 0.1$ (Fig. 4) their maximum values occur far from the duct center. It is concluded that as the aspect ratio H/W is reduced the velocity overshooting appears at smaller δ and/or larger θ.

4.2 Flow rates

The behavior of the oscillatory flow rates $\hat{G} = G_A \cos\left(t - G_P\right)$ in terms of δ, θ, the aspect ratio H/W and the accommodation coefficient α is investigated.

In Fig. 5, the flow rate amplitude G_A and phase angle G_P are provided in terms of δ with $\theta = \left[1, 10, 10^2\right]$ and $H/W = \left[1, 0.5, 0.1, 0\right]$. The case of $H/W = 0$ corresponds to oscillatory flow between parallel plates. Purely diffuse reflection is assumed at the wall ($\alpha = 1$). It is clearly seen that θ has a strong effect on the amplitude G_A, while its effect on G_P is very weak. More specifically, for $\theta = 1$, G_A is monotonically decreased as δ is increased, while for $\theta = \left[10, 10^2\right]$ it is initially decreased, then it is increased up to some local maximum appearing at $\delta \in \left[5, 15\right]$ and finally it is decreased. This behavior is justified by the fact that at adequately high oscillation frequencies (e.g., $\theta = 1$), G_A is significantly affected and it is monotonically reduced with increasing δ. On the contrary at low oscillation frequencies (e.g., $\theta = \left[10, 10^2\right]$), the variation of G_A with δ has some resemblance with the steady flow rate including the presence of a Knudsen minimum, as long as δ is sufficiently small to ensure $\delta << \theta$. Then, as δ is further increased the inequality does not hold and G_A is decreased. With regard to the phase angle, G_P is always monotonically increased with δ and it is almost independent of the oscillation frequency θ. At very small values of δ it is almost zero, then at moderate values of δ it is rapidly increased and finally, at large values of δ it is asymptotically increased

reaching the limiting value of $\pi/2$.The described behavior of G_A and G_P with regard to δ and θ is qualitatively the same in all aspect ratios H/W. It is clear however, that the aspect ratio has quantitatively a significant effect on G_A and a weak effect on G_P, which becomes even weaker as θ is increased and the flow becomes stationary. In general, G_A is always increased as H/W is decreased and this is more evident for $\delta < 1$. Concerning the value of the local maximum of G_A at large θ within some $\delta \in [5,15]$ again it is increased as the aspect ratio H/W is decreased obtaining the maximum value in the case of flow between parallel plates ($H/W = 0$).

In Fig. 6, the flow rate amplitude G_A and phase angle G_P are provided in terms of δ with $\theta = [0.1,1,10]$, $H/W = [1,0.1]$ and the accommodation coefficient $\alpha = [1,0.85,0.7]$. As expected, $G_A(\delta,\theta)$ is monotonically increased as α is increased, i.e., the reflection becomes more specular. The phase angle G_P however, does not strongly depend on the type of gas-surface interaction. As α is decreased the phase angle lag is only slightly increased for the same δ and θ, which becomes more evident as θ is decreased and at moderate values of δ.

In Fig. 7, the oscillatory flow rate $\hat{G} = G_A \cos(t - G_P)$, is plotted versus time $t \in [0, 2\pi]$ for typical values of δ and θ with $H/W = [1,0.1]$. The time evolution of the dimensionless pressure gradient is equal to $\cos t$. It is seen that $\hat{G}$ strongly depends on both the gas rarefaction parameter and the oscillation frequency. When $\delta = 0.1$, the $\hat{G}$ profiles for $\theta = [1,10,10^2]$ (low and moderate oscillation frequencies) are very close to each and in phase with the pressure gradient, while for $\theta = 0.1$ (high oscillation frequency) $\hat{G}$ has a smaller amplitude and a larger lagging phase angle. As δ is increased the effect of θ becomes gradually more dominant. At $\delta = 1$, the $\hat{G}$ profiles only for $\theta = [10,10^2]$ are close to each other and in phase, while for $\theta = [0.1,1]$ the amplitude is reduced and the phase angle lag is increased. This behavior is further enhanced at $\delta = 10$, where the effect of the oscillation frequency is very significant for $\theta = [0.1,1,10]$ and remains not important only for $\theta = 10^2$. It is seen that at $\delta = 1$ and

$\theta = 0.1$, as well as at $\delta = 10$ and $\theta = 0.1,1$ the amplitudes are very small and the phase angle lags are almost $\pi/2$. These observations are valid for both aspect ratios. Quantitatively, as H/W is decreased moving from the square duct to the parallel plates setup the amplitude is increased and the phase angle lag is slightly increased, which is in agreement with the observations in Fig. 6. It is also noted that the peak of the flow rate amplitude always falls short of reaching the corresponding steady flow rate, which is clearly contributed to the inertia of the fluid, which must be accelerated and decelerated in each cycle.

Tabulated results of the flow rate amplitude G_A and phase angle G_P for the specific case of an orthogonal duct with $H/W = 0.1$ are presented in Tables 1 and 2 respectively in terms of the gas rarefaction $\delta \in \left[10^{-4}, 10^{2}\right]$ and the oscillation parameter $\theta = \left[0.1,1,10,50,10^{2}\right]$. In addition, the flow rate amplitude $G_A^{(S)}$ and phase angle $G_P^{(S)}$ in the slip regime, based on the analytical expression (B10), are provided for $\delta \geq 1$ with $\theta = 50$ and $\theta = 10^2$. In the last column of Table 1, the well-known steady flow rates ($\theta \to \infty$), denoted by $G_S(\delta)$, for $\delta \leq 15$ are also included [41]. By comparing G_A and G_P with the corresponding $G_A^{(S)}$ and $G_P^{(S)}$ it is readily seen that there is very good agreement up to at least two significant figures for $\delta > 10$ (both δ and θ must be large) and then, as δ is decreased the discrepancies are gradually increased. Also, the values $G_A(\delta,\theta)$ for the large oscillation parameter $\theta = 10^2$ are in very good agreement with the corresponding steady flow rates $G_S(\delta)$ in small and intermediate values of δ and then, as δ is further increased the discrepancies also increase. This is expected since steady conditions are recovered provided that the oscillation parameter is large (which it is, since $\theta = 10^2$) and also $\delta << \theta$ (which is the case only when $\delta < 10$). These comparisons demonstrate the accuracy of the kinetic results.

Furthermore, it is seen in Table 1 that for any given δ, G_A is monotonically increased with θ, being always less than the corresponding stationary solution $G_S(\delta)$. Also, as δ is increased, for $\theta \leq 1$, G_A is monotonically decreased, while for $\theta \geq 10$ it is initially decreased until $\delta = 1$, where a local minimum is observed, then it is increased up

to some δ, which depends on θ, and finally as δ is further increased it is again decreased. As $\delta \to 0$ and for all θ, the solution tends to the semi-analytical steady free molecular flow rate, which is equal to 1.991 (see Table II in [41]). For small values of θ and adequately large values of δ, G_A tends to diminish, since due to the high oscillation frequency and the deduced inertial forces the gas has great difficulty to reach a peak flow.

In Table 2, for any given δ the phase angle G_P is increased as θ is decreased, i.e., as the oscillation frequency is increased. At very high frequencies and adequately large δ, this may result to almost zero amplitude with $\pi/2$ phase angle. Also, for any given θ, G_P is monotonically increased with δ, being almost zero in the free molecular regime and then, it is increasing as the oscillatory flow becomes less rarefied, reaching the maximum phase angle lag in the hydrodynamic limit. Overall, as the oscillation frequency is increased the flow rate amplitude is decreased, while the phase angle is increased, which in accordance with the observations made in Section 4.1 for the velocity distributions.

4.3 Mean wall shear stresses and acting forces

Next, the behavior of the oscillatory mean wall shear stress $\bar{\hat{\tau}}_W = \bar{\tau}_{W,A}\cos\left(t - \bar{\tau}_{W,P}\right)$ in terms of δ, θ and H/W is investigated. It is noted that the steady mean wall shear stress $\bar{\tau}_{S,W} = 0.25\left(1 + H/W\right)^{-1}$ is independent of δ and depends only on the aspect ratio H/W (Section2, Eq. (29)).

In Fig. 8, the oscillatory mean wall shear stress amplitude $\bar{\tau}_{W,A}$ and phase angle $\bar{\tau}_{W,P}\left(\delta,\theta\right)$ are plotted in terms of δ with $\theta = \left[1, 10, 10^2\right]$ and $H/W = \left[1, 0.5, 0.1, 0\right]$. For very small values of δ the mean wall shear stress amplitude $\bar{\tau}_{W,A}$ takes the same value as the corresponding steady one $\bar{\tau}_{S,W}$ at the same H/W. Then, as δ is increased it is slightly reduced and then, from some δ in the late transition or slip regimes it is rapidly decreased. The value of δ where this rapid decrease of $\bar{\tau}_{W,A}$ is starting depends on θ and it is increasing as θ is decreasing. At $\theta = \left[1, 10, 10^2\right]$ the corresponding values of δ are

about $\delta=[0.1,2,10]$. Thus, the variation of $\overline{\tau}_{W,A}$ does not include the local maxima observed in the variation of G_A (Fig. 5). This overall behavior of $\overline{\tau}_{W,A}$ is valid for all values of the aspect ratio H/W. Also, it is seen that $\overline{\tau}_{W,A}$ depends strongly on the aspect ratio, particularly in the free molecular and slip regimes and it is always increased as H/W is decreased. The dependency of the oscillatory mean wall shear stress phase angle $\overline{\tau}_{W,P}$ on δ, θ and H/W is very close to the corresponding one of the flow rate phase angle G_P in Fig. 5. More specifically, it is increased with δ having a rapid increase in the transition regime, it is also increased as θ is decreased and finally, it demonstrates a weak dependency on H/W.

It is noted that comparing the corresponding phase angle lags $\overline{\tau}_{W,P}$ and G_P, it has been found (although it is not clearly seen in Figs. 5 and 8) that $\overline{\tau}_{W,P}$ is almost always slightly smaller than G_P deducing that the mean wall shear stress has a smaller phase angle lag than the flow rate. This observation is always true in the slip and hydrodynamic regimes [4,5]. It has been found however, that in some narrow band of the transition regime close to $\delta \square 1$ and high oscillation frequency $\theta \le 1$, $\overline{\tau}_{W,P}$ may be slightly larger than G_P.

In Fig. 9, the oscillatory shear stress $\tilde{\tilde{\tau}}_W(t,\delta,\theta)=\overline{\tau}_{W,A}\cos(t-\overline{\tau}_P)$ is plotted versus time $t\in[0,2\pi]$ for typical values of δ and θ with $H/W=[1,0.1]$. The time evolution of the dimensionless pressure gradient is equal to $\cos t$. As expected, $\tilde{\tilde{\tau}}_W$ depends on both the gas rarefaction parameter and the oscillation frequency and behaves similarly to the flow rate $\hat{G}$ (Fig. 7). As θ is decreased the amplitude is decreased and the lagging phase angle is increased and this behavior becomes more intense as δ is increased. Furthermore, as H/W is decreased, the amplitude is increased, while the phase angle is slightly increased.

Next in Fig. 10, the oscillatory inertia, $\hat{F}_I$, viscous $\hat{F}_V$ and pressure $\hat{F}_P$ forces, as defined in Eq. (30) are plotted over one oscillation period $t\in[0,2\pi]$ for $\delta=[0.1,1,10]$, $\theta=[0.1,1,10]$ and $H/W=1$. The forces are readily computed based on the amplitudes and phase angles of the flow rate and mean wall shear stress. In all cases the force balance

equation (30) is satisfied. The inertia forces refer to the core flow and the viscous forces refer to the Stokes layer. It is interesting to observe the behavior of $\hat{F}_I$ and $\hat{F}_V$ in terms of δ and θ. The phase difference between these two forces is always $\pi/2$. In the cases of $(\delta=\theta=0.1)$, $(\delta=\theta=1)$ and $(\delta=\theta=10)$ the viscous and inertia forces lag and lead the corresponding pressure force respectively by a phase angle of $\pi/4$. The amplitudes of the two forces are about the same. Then, in the cases of $(\delta=10,\ \theta=1,0.1)$ and $(\delta=1,\ \theta=0.1)$, the inertia forces almost coincide with the corresponding pressure forces, while the viscous forces lag the other two forces by almost $\pi/2$ and their amplitudes are close to zero. The flow consists of two regions: the core region oscillating in a plug mode and, adjacent to the wall, the oscillating thin viscous or Stokes layer with the velocity overshooting. Finally, in the cases of $(\delta=1,\ \theta=10)$ and $(\delta=0.1,\ \theta=1,10)$ this behavior is reversed, i.e., the viscous coincide with pressure forces, while the inertia forces lead by almost $\pi/2$ and their amplitudes are close to zero. The flow consists of one oscillating region with no velocity overshooting. This description clarifies the behavior of the inertia and viscous forces in terms of θ and more important in terms of δ, e.g., at $\delta=10$ and $\theta\le 1$ the flow is dominated mainly by inertia forces, while at $\delta=0.1$, the flow will be dominated by inertia forces only if $\theta<0.1$.

It is noted finally, that based on the computed quantities, Eq. (30) is satisfied very accurately, which of course provides additional confidence about the validity of the numerical results.

4.4 Pumping power

In Fig. 11, the oscillatory pumping power, defined as $\hat{E}/(Adz)=$ $=G_A\cos(G_P-t)\cos t/2$ (see Eq. (31)), is plotted in terms of $t\in[0,2\pi]$ for $\delta=[0.1,1,10]$ and $\theta=[0.1,1,10,10^2]$ with $H/W=0.1$. The pumping power has two peaks within each oscillatory cycle because it consists of the product of the oscillatory pressure times the oscillatory flow. Its integral over one cycle is not zero in order to drive the oscillatory flow, although the oscillatory net flow is zero. The dependency of the

oscillatory pumping power on δ and θ is similar to the one observed for the flow rate, i.e. in general, as θ is decreased (the oscillation frequency is increased) its amplitude is decreased and its phase angle lag is increased. This behavior becomes more dominant as δ is increased.

As pointed above, even when the flow is reversed, which is occurring at the second half of the oscillation cycle at time $t \in [\pi/2, \pi]$ where the flow rate is negative, the pumping power remains positive. It is seen however, in Fig.11 that at certain times $t \in [0, 2\pi]$, the oscillatory pumping power may become negative. This is more evident at large δ and small θ and it is occurring because in dense gases and at relatively high frequencies the flow rate is completely out of phase with the pressure gradient (it becomes proportional to a sinusoidal function). Thus, when the pressure gradient becomes negative and the flow is reversed, the sign of the flow rate remains positive for a certain time interval and during this interval the overall pumping power becomes negative. This time interval is increased as θ is decreased. Of course in rarefied gases and/or low frequencies $\hat{E}$ is always positive because the flow rate is in phase with the pressure gradient.

Finally, in Fig. 12, the average oscillatory pumping power $\overline{E} / Adz = G_A \cos(G_P)/4$ (see Eq. 32) over one period of oscillation in terms of δ are plotted, with $\theta = [0.1, 1, 10, 10^2]$ and for ducts with $H/W = 1$ and 0.1. The steady pumping power $E_S = AdzG_S/2$, which depends only on δ, is also plotted for comparison purposes. It is seen that as the oscillatory flow approaches steady conditions, which is the case of $\theta = 10^2$ and $\delta \le 10$, as expected, $\overline{E}$ is about half of E_S. This behaviour is even extended to smaller values of θ provided that δ is adequately small ($\delta << \theta$). Also, as $\delta \to 0$ and for all θ the steady free molecular flow is recovered, $\overline{E}$ is exactly one half of the steady free molecular pumping power. Furthermore, in cases where $\delta \ge \theta$ the average oscillatory pumping power is smaller than these limiting values and it is significantly decreased with θ. This is expected since at very high frequencies the flow rate amplitude tends to diminish. Also, the local maximum values of $\overline{E}$ at large θ are appearing due to the corresponding behaviour of G_A, shown in Fig. 5. With regards to the aspect ratio, $\overline{E}$ is increased as H/W is increased.

5. Concluding remarks

The pulsatile isothermal fully-developed flow in an orthogonal duct is investigated by decomposing the flow into the steady and oscillatory parts. The steady part is well-known and therefore, the investigation is focused mainly on the oscillatory part, which is numerically solved, based on the time-dependent linear BGK equation, in a wide range of the gas rarefaction parameter $\delta \in \left[0,10^2\right]$ and the oscillation parameter $\theta \in \left[10^{-2},10^2\right]$, as well as for various values of the duct aspect ratio $H/W \in \left[1,0\right]$ and the tangential momentum accommodation coefficient $\alpha \in \left[0,1\right]$. It is noted that δ and θ are inversely proportional to the Knudsen number and the oscillation frequency respectively. The results are in dimensionless form and include all macroscopic quantities of theoretical and technological interest and more specifically, the amplitude and phase angle, as well as the time evolution of the velocity distribution, the flow rate, the mean wall shear stress, the acting inertial and viscous forces, the pumping power and the time average pumping power. The results have been successfully validated at limiting values of δ and θ by comparison with corresponding analytical results in the slip regime (both $\delta >> 1$ and $\theta >> 1$), in the free molecular regime ($\delta \to 0$) and with numerical results for steady fully-developed flow ($\theta \to \infty$ and $\delta << \theta$).

Always as θ is decreased (i.e., the oscillation frequency is increased) the amplitude of all macroscopic quantities is decreased and their phase angle lag with respect to the pressure gradient is increased. Actually, at very small θ the amplitude tends to diminish and the phase angle lag approaches the limiting value of $\pi/2$. It is important to note however, that as δ is decreased (i.e., the gas becomes more rarefied) higher frequencies are needed to trigger the behavior described above.

For comparison purposes the amplitude of the oscillatory pressure gradient is taken to be equal with the steady pressure gradient. Having this in mind it is useful to note that the pulsatile velocity distribution, which is obtained by adding the oscillatory and steady velocities, is always positive and therefore, there is no flow reversal. Furthermore, the amplitudes of the flow rate and the mean wall shear stress are increased with θ being always smaller than the corresponding steady ones. In terms of gas rarefaction the

dependency of the flow rate amplitude is not monotonic indicating that at moderate and large θ there is a critical δ to obtain the maximum flow rate. The mean wall shear stress amplitude remains almost constant in the free molecular and transition regimes and then it is rapidly reduced. Comparing the corresponding phase angle lags of the flow rate and the mean wall shear stress it has been found that in most cases the former one is slightly larger, while this situation is reversed in a narrow band of the transition regime and high oscillation frequencies. Concerning the duct aspect ratio it has been found that as the aspect ratio H/W is decreased the flow rate and mean wall shear stress amplitudes are increased, while their phase angle lags are slightly affected. Similarly, the gas-surface interaction at the wall, specified by the accommodation coefficient α, has a significant effect at the amplitudes and almost no effect at the phase angles of the macroscopic quantities.

The inertia and viscous forces, having always a phase difference of $\pi/2$, are computed in a wide range of δ and θ. Their amplitudes are about the same when $\delta = \theta$. As δ is increased and θ is decreased the inertia forces dominate causing a core oscillating plug-flow with a thin Stokes layer. In the opposite situation (i.e., as δ is decreased and θ is increased) the viscous forces become more important causing a typical viscous oscillatory flow without velocity overshooting.

Finally, the oscillatory pumping power has two peaks within each oscillatory cycle and its integral over one cycle is not zero. The nonzero time average pumping power is needed to maintain the oscillatory flow, although the oscillatory net flow is zero and it is increased as the oscillation frequency is reduced. Actually, as stationary conditions are reached, the time average pumping power is obtaining its maximum values, which have been found to be one half of the corresponding steady ones. Adding the time average oscillatory pumping power with the steady one, yields the total average power to maintain the pulsatile flow.

Acknowledgements

This work has been carried out within the framework of the EUROfusion Consortium and has received funding from the Euratom research and training programme 2014-2018

under grant agreement No 633053 (WP: EDU). The views and opinions expressed herein do not necessarily reflect those of the European Commission.

Appendix A. Kinetic formulation of the pulsatile flow between parallel plates

In the specific case of $H/W=0$ the flow setup is reduced to pulsatile flow between two parallel plates and it is modeled by the one-dimensional time-dependent BGK model in the domain $-1/2\le y\le 1/2$. Following a mathematical manipulation similar to the one presented in Section 3, the steady and oscillatory parts of the pulsatile flow are modeled. The steady part results to the well-known kinetic formulation of steady Poiseuille flow between parallel plates [40]. The oscillatory part results to the following equations:

$$c_y\frac{\partial h}{\partial y}+h\left(\delta-\frac{\delta}{\theta}i\right)+c_z=2\delta c_z u(y) \tag{A1}$$

$$u(y)=\frac{1}{\pi^{3/2}}\int_{-\infty}^{\infty}\int_{-\infty}^{\infty}\int_{-\infty}^{\infty}c_z h e^{-c^2}dc_x dc_y dc_z \tag{A2}$$

$$\tau_{xz}(y)=\frac{1}{\pi^{3/2}}\int_{-\infty}^{\infty}\int_{-\infty}^{\infty}\int_{-\infty}^{\infty}c_y c_z h e^{-c^2}dc_x dc_y dc_z \tag{A3}$$

Next, the c_x and c_z components of the molecular velocity vector are eliminated by introducing the reduced distribution function

$$Y(y,c_y)=\frac{1}{\pi}\int_{-\infty}^{\infty}\int_{-\infty}^{\infty}h(x,c_x,c_y,c_z)\exp\left[-{c_z}^2-{c_x}^2\right]dc_x dc_z\,. \tag{A4}$$

Equation (A1) is multiplied by $c_x c_z\exp\left(-c_x^2-c_z^2\right)/\pi$ and the resulting equation is integrated over c_x and c_z to deduce

$$c_y\frac{\partial Y}{\partial y}+\left(\delta-i\frac{\delta}{\theta}\right)Y(y,c_y)=\delta u(y)-\frac{1}{2} \tag{A5}$$

with Y being a complex function, while the velocity and shear stress distributions are

$$u(y)=\frac{1}{\sqrt{\pi}}\int_{-\infty}^{\infty}Ye^{-c_y^2}dc_y \qquad \text{and} \qquad \tau(y)=\frac{1}{\sqrt{\pi}}\int_{-\infty}^{\infty}c_y Ye^{-c_y^2}dc_y \tag{A6}$$

The Maxwell diffuse-specular boundary conditions become

$$Y^{+}\left(\mp 1/2,c_y\right)=(1-\alpha)Y^{-}\left(\mp 1/2,c_y\right),\ c_x\ ¤\ 0. \tag{A7}$$

The one-dimensional oscillatory flow problem ($H/W=0$), defined by Eqs. (A5-A7), is solved in order to have a complete view of the effect of the channel aspect ratio $H/W\in[0,1]$ on the oscillatory flow characteristics.

Appendix B. Analytical solutions in the hydrodynamic and slip regimes

The hydrodynamic and slip regimes are characterized by large values of both flow parameters δ and θ. As $\delta\to\infty$ and $\theta\to\infty$, by retaining the fully-developed flow assumption the continuity equation is identically satisfied and the $z-$momentum equation becomes [3,4,17]

$$\rho\frac{\partial\hat{U}_{PUL}^{(m)}}{\partial t'}=-\frac{d\hat{P}_{PUL}}{dz'}+\mu\left(\frac{\partial^2\hat{U}_{PUL}^{(m)}}{\partial x'^2}+\frac{\partial^2\hat{U}_{PUL}^{(m)}}{\partial y'}\right), \tag{B1}$$

where the pressure gradient $d\hat{P}_{PUL}\left(z',t'\right)/dz'$ and velocity $\hat{U}_{PUL}^{(m)}\left(t',x',y'\right)$, with $m=H,S$ denoting the hydrodynamic and slip solutions, are defined by Eqs. (1) and (2) respectively. The pressure gradient and the velocity are decomposed into the steady and oscillatory parts. The former one yields the steady Stokes equation and the latter one may be written in dimensionless form as

$$\frac{\partial^2u^{(m)}}{\partial y^2}+\frac{\partial^2u^{(m)}}{\partial x^2}+2i\frac{\delta^2}{\theta}u^{(m)}=-\delta, \tag{B2}$$

where $u^{(m)}=u^{(m)}\left(x,y\right)$, $m=H,S$, is the complex hydrodynamic or slip velocity. Equation (B2) is also known as the unsteady Stokes equation. The steady and unsteady Stokes equations subject to no-slip and slip boundary conditions have been solved analytically in [47] and [17] respectively. Here, we are interested mainly to the oscillatory flow and therefore, the solution of Eq. (B2) is provided in terms of the present notation without however describing the methodology.

In the hydrodynamic regime ($m=H$), Eq. (B2) subject to the associated no-slip boundary conditions $u\left(x,\pm1/2\right)=0$ and $u\left(\pm H/2W,y\right)=0$ is solved to yield

$$u^{(H)}=4\delta\sum_{j=0}^{\infty}\frac{\sin\left(b_j/2\right)}{b_j{p_j}^2}\left[1-\cosh\left(p_jx\right)\Big/\cosh\left(\frac{W}{2H}p_j\right)\right]\cos\left(b_jy\right), \tag{B3}$$

where $b_j = (2j+1)\pi$, $j = 0,1,2,3,...$ and $p_j = \sqrt{b_j^2 - 2i\delta^2/\theta}$. The velocity field is integrated according to Eq. (22) to find the hydrodynamic flow rate

$$G^{(H)} = 8\delta \sum_{j=0}^{\infty} \frac{1-\cos b_j}{b_j^2 p_j^2} \left[p_j - \frac{2H}{W} \tanh\left(\frac{W}{2H} p_j \right) \right]. \tag{B4}$$

Then, the velocity field is differentiated with respect to x and y to find the shear stresses

$$\tau_{xz}^{(H)} = -2 \sum_{j=0}^{\infty} \frac{\sin(b_j/2)}{b_j p_j} \left[1 - \sinh(p_j x) \Big/ \cosh\left(\frac{W}{2H} p_j \right) \right] \cos(b_j y) \tag{B5}$$

and

$$\tau_{yz}^{(H)} = -2 \sum_{j=0}^{\infty} \frac{\sin(b_j/2)}{p_j^2} \left[1 - \cosh(p_j x) \Big/ \cosh\left(\frac{W}{2H} p_j \right) \right] \sin(b_j y). \tag{B6}$$

In the slip regime ($m = S$), Eq. (B2) subject to the associated slip boundary conditions [17]

$$u^{(S)}(x, \pm 1/2) = \mp \frac{\sigma_P}{\delta} \frac{du^{(S)}}{dy}\bigg|_{y=\pm 1/2} \quad \text{and} \quad u^{(S)}(\pm H/(2W), y) = \mp \frac{\sigma_P}{\delta} \frac{du^{(S)}}{dx}\bigg|_{x=H/(2W)} \tag{B7}$$

where $\sigma_P = 1.016$ is the viscous slip coefficient is solved to yield

$$u^{(S)} = 4\delta \sum_{j=0}^{\infty} \frac{\sin(b_j/2)\cos(b_j y)}{b_j p_j^2 \left(1 + 2\frac{\sigma_P}{\delta} \sin^2(b_j/2) \right)} \left[1 - \frac{\cosh(p_j x)}{\cosh\left(\frac{W}{2H} p_j \right) + \frac{\sigma_P}{\delta} p_j \sinh\left(\frac{W}{2H} p_j \right)} \right] \tag{B8}$$

In Eq. (B8) $p_j = \sqrt{b_j^2 - 2i\delta^2/\theta}$, while the eigenvalues b_j are the roots of the trascedental equation $b_j \tan(b_j/2) = \delta/\sigma_P$. Then, the slip flow rate and shear stresses are

$$G^{(S)} = 8\delta \sum_{j=0}^{\infty} \frac{1-\cos b_j}{b_j^2 p_j^3 \left(1 + 2\frac{\sigma_P}{\delta} \sin^2(b_j/2) \right)} \left(p_j - \frac{2H}{W} \frac{1}{\coth\left(\frac{W}{2H} p_j \right) + \frac{\sigma_P}{\delta} p_j} \right) \tag{B10}$$

$$\tau_{xz}^{(S)} = -2 \sum_{j=0}^{\infty} \frac{\sin(b_j/2)\cos(b_j y)\sinh(p_j x)}{b_j p_j \left[1 + 2\frac{\sigma_P}{\delta} \sin^2(b_j/2) \right] \left[\cosh\left(\frac{W}{2H} p_j \right) + \frac{\sigma_P}{\delta} p_j \sinh\left(\frac{W}{2H} p_j \right) \right]} \tag{B11}$$

$$\tau_{yz}^{(S)} = -2\sum_{j=0}^{\infty} \frac{\sin\left(b_j/2\right)\cos\left(b_j y\right)}{p_j^2\left(1+2\frac{\sigma_P}{\delta}\sin^2\left(b_j/2\right)\right)}\left[1-\frac{\cosh\left(p_j x\right)}{\cosh\left(\frac{W}{2H}p_j\right)+\frac{\sigma_P}{\delta}p_j\sinh\left(\frac{W}{2H}p_j\right)}\right] \quad \text{(B12)}$$

The closed form expressions (B4-B6) and (B10-B11) are implemented to validate the kinetic solution for large values of both δ and θ.

References

1. F. M. White, *Viscous Fluid Flow*, (McGraw Hill, New York), 143-145, 1974.
2. H. Schlichting and K. Gersten, *Boundary-layer Theory,* (Springer, Berlin), 137-139, 2017.
3. D. G. Drake, On the flow in a channel due to the periodic pressure gradient, *The Quarterly Journal of Mechanics and Applied Mathematics*, 18 (1), 1-10, 1965.
4. M. Zamir, *Physics of Pulsatile Flow*, Springer–Verlag, New York, 2000.
5. S. Uchida, The pulsating viscous flow superposed on the steady laminar motion of incompressible fluid in a circular pipe, Zeitschrift fur angewandte Mathematik und Physik ZAMP, 7 (5), 403–422, 1956.
6. H. Ito, Theory of laminar flow through a pipe with non-steady pressure gradients, *Transactions of the Japan Society of Mechanical Engineers*, 18 (66), 101-108, 1953.
7. C. Fan and B. Chao, Unsteady, laminar, incompressible flow through rectangular ducts, Zeitschrift f¨urangewandte Mathematik und Physik ZAMP, 16 (3), 351–360, 1965.
8. N. Rott, Theory of Time-Dependent Laminar Flows, *Theory of Laminar Flows*, F. K. Moore (Ed.), (Princeton University Press, Princeton), pp. 395–438, 1964.
9. S. T. Zhao and P. Cheng, Friction Coefficient of a Fully Developed Laminar Reciprocating Flow in a Circular Pipe, International Journal of Heat and Fluid Flow, 17 (2), 167–172, 1996.
10. J. Majdalani, Exact Navier–Stokes solution for pulsatory viscous channel flow with arbitrary pressure gradient, Journal of Propulsion and Power, 24 (6), 1412-1423, 2008.
11. R. Blythman, N. Jeffers, T. Persoons, and D. Murray, Effect of oscillation frequency on wall shear stress and pressure drop in a rectangular channel for heat transfer applications, Journal of Physics: Conference Series: 745, 032044, 2016.
12. R. Blythman, T. Persoons, N. Jeffers, K. P. Nolan and D. B. Murray, Localized dynamics of laminar pulsatile flow in a rectangular channel, International Journal of Heat and Fluid Flow, 66, 8-17, 2017.
13. R. Caen and S. Colin, Multidirectional pneumatic force sensor for grippers, Robotic Systems, 10, 551-558, 1992.
14. R. A. Abreu, A. P. Troup and M. K. Sahm, Causes of anomalous solid formation in the exhaust systems of low-pressure chemical vapor deposition and plasma enhanced chemical vapor deposition semiconductor processes, Journal of Vacuum Science and technology B, 12 (4), 2763-2767, 1994.

15. A. Batikh, R. Caen, S. Colin, L. Baldas, A. Kourta and H. C. Boisson, Numerical and experimental study of micro synthetic jets for active flow control, International Journal of Heat and Technology, 26 (1), 139-145, 2008.
16. S. Wang, L. Baldas, S. Colin, A. Kourta and N. Mazellier, Numerical and experimental characterization of a micro-oscillator for flow control, Proceedings of the 4th European Conference on Microfluidics, Limerick, December 10-12, 2014.
17. S. Colin, C. Aubert and R. Caen, Unsteady gaseous flows in rectangular microchannels: frequency response of one or two pneumatic lines connected in series, European Journal of Mechanics B/Fluids, 17, 79-104, 1998.
18. C. Cercignani, *The Boltzmann Equation and its Applications*, (Springer, New York), 1988.
19. P. L. Bhatnagar, E. P. Gross and M. A. Krook, A model for collision processes in gases, Physical Review, 94, 511–525, 1954.
20. L. H. Holway, New statistical models for kinetic theory: Methods of construction, Physics of Fluids, 9 (9), 1658-1673, 1966.
21. E. M. Shakhov, Generalization of the Krook kinetic relaxation equation, Fluid Dynamics, 3 (5), 95-96, 1968.
22. A. Tsimpoukis and D. Valougeorgis. Rarefied isothermal gas flow in a long circular tube due to oscillating pressure gradient, Microfluidics and Nanofluidics, 22, 5, 2018.
23. F. Sharipov and D. Kalempa, Oscillatory flow at arbitrary oscillation frequency over the whole range of the Knudsen number, Microfluid Nanofluid, 4, 363-374, 2008.
24. D. Kalempa and F. Sharipov, Sound propagation through a rarefied gas confined between source and receptor at arbitrary Knudsen number and source frequency, Physics of Fluids, 21, 103601, 2009.
25. F. Sharipov and D. Kalempa, Gas flow near a plate oscillating longitudinally with an arbitrary frequency, Physics of Fluids, 19, 107110, 2007.
26. J. H. Park, P. Bahukudumbi and A. Beskok, Rarefaction effects on shear driven oscillatory gas flows: A direct simulation Monte Carlo study in the entire Knudsen regime, Physics of Fluids, 16 (2), 317–330, 2004.
27. N. G. Hadjiconstantinou, Oscillatory shear-driven gas flows in the transition and free-molecular flow regimes, Physics of Fluids, 17 (100), 611–619, 2005.
28. A. Manela and L. Pogorelyuk, Cloaking via heating: Approach to acoustic cloaking of an actuated boundary in a rarefied gas, Physic of Fluids, 26, 062003, 2014.
29. A. Manela, G. A. Radtke and L. Pogorelyuk, On the damping effect of gas rarefaction on propagation of acoustic waves in a microchannel, Physic of Fluids, 26, 032001, 2014.
30. L. Wu, J. M. Reese and Y. Zhang, Oscillatory rarefied gas flow inside rectangular cavities, Journal of Fluid Mechanics, 748, 350-367, 2014.
31. L. Wu, Sound propagation through a rarefied gas in rectangular channels, Physical Review E, 94, 053110, 2016.
32. D. R. Emerson, X. J. Gu, S. K. Stefanov, S. Yuhong and R. W. Barber, Nonplanar oscillatory shear flow: From the continuum to the free-molecular regime, Physics of Fluids, 19, 107105, 2007.
33. L. Desvillettes and S. Lorenzani, Sound wave resonance in micro-electro-mechanical systems devices vibrating at high frequencies according to the kinetic theory of gases, Physics of Fluids, 24, 092001, 2012.

34. C. M. Ho and Y. C. Tai, Micro-electro-mechanical systems and fluid flows, Annual Review in Fluid Mechanics, 30, 579-612, 1998.
35. A. Frangi, A. Frezzotti and S. Lorenzani, On the application of the BGK kinetic model to the analysis of gas-structure interactions in MEMS, Computers and Structures, 85, 810–817, 2007.
36. T. Veijola, Compact Models for Squeezed-Film Dampers with Inertial and Rarefied Gas Effects, Journal of Micromechanics and Microengineering, 14, 1109–1118, 2004.
37. T. Veijola and A. Lehtovuori, Numerical and analytical modelling of trapped gas in micromechanical squeeze-film dampers, Journal of Sound Vibration, 319, 606-621, 2009.
38. A. Gallis and R. Torczynski, An improved Reynolds-equation model for gas damping of microbeam motion, Journal of Microelectromechanical Systems, 13, 653–659, 2004.
39. X. Guo and A. Alexeenko, Compact model of squeeze-film damping based on rarefied flow simulations, Journal of Micromechanics and Microengineering, 19, 045026, 2009.
40. F. Sharipov, *Rarefied Gas Dynamics. Fundamentals for Research and Practice*, Wiley-VCH, 2016.
41. F. Sharipov, Rarefied gas flow through a long rectangular channel**,** Journal of Vacuum Science & Technology A, 17 (5), 1999.
42. S. Pantazis, S. Varoutis, V. Hauer, C. Day, D. Valougeorgis, Gas-surface scattering effect on vacuum gas flows through rectangular channels, Vacuum, 85, 12, 1161-1164, 2011.
43. S. Varoutis, J. Lihnaropoulos, D. Mathioulakis, A. Tserepi and D. Valougeorgis, Estimation of the Poiseuille number and of the exact hydraulic diameter in rarefied gas flows through channels of various cross sections, 1st European Conference on Microfluidics (mFlu'08), Bologna, Italy, 2008.
44. S. Naris and D. Valougeorgis, Rarefied gas flow in a triangular duct based on a boundary fitted lattice, European Journal of Mechanics B/Fluids, 27, 810-822, 2008.
45. J. Lihnaropoulos and D. Valougeorgis, Unsteady vacuum gas flow in cylindrical tubes, Fusion Engineering and Design, 86, 2139–2142, 2011.
46. O. Buchina and D. Valougeorgis, Oscillatory heating in a microchannel at arbitrary oscillation frequency in the whole range of the Knudsen number, Journal of Physics: Conference Series 362, 012015, 2012.
47. W. A. Ebert and E. M. Sparrow, Slip flow in rectangular and annular ducts, ASME Journal of Basic Engineering, 87, 1018-1024, 1965.

Table 1: Flow rate amplitude $G_A(\delta,\theta)$ in terms of gas rarefaction parameter δ and oscillation parameter θ for $H/W=0.1$

δ	$G_A(\delta,\theta)$					$G_A^{(S)}(\delta,\theta)$		$G_{SS}(\delta)$
	$\theta=0.1$	$\theta=1$	$\theta=10$	$\theta=50$	$\theta=100$	$\theta=50$	$\theta=100$	$\theta\to\infty$
0.0001	1.984	1.988	1.988	1.988	1.988			1.988
0.001	1.939	1.973	1.974	1.974	1.974			1.974
0.01	1.648	1.892	1.903	1.903	1.903			1.903
0.05	1.057	1.712	1.758	1.759	1.759			1.759
0.1	7.543(-1)	1.583	1.666	1.667	1.667			1.667
0.5	2.033(-1)	1.116	1.451	1.456	1.456			1.456
1	9.992(-2)	8.084(-1)	1.411	1.426	1.427	1.104	1.104	1.427
2	4.999(-2)	4.793(-1)	1.431	1.492	1.494	1.263	1.265	1.494
4	2.499(-2)	2.462(-1)	1.414	1.719	1.732	1.567	1.578	1.737
6	1.666(-2)	1.646(-1)	1.245	1.952	1.999	1.841	1.881	2.016
8	1.250(-2)	1.237(-1)	1.042	2.142	2.262	2.059	2.168	2.307
10	9.999(-3)	9.914(-2)	8.720(-1)	2.259	2.503	2.198	2.428	2.605
15	6.666(-3)	6.627(-2)	6.043(-1)	2.216	2.918	2.191	2.874	3.364
20	5.000(-3)	4.977(-2)	4.622(-1)	1.931	2.989	1.920	2.966	
30	3.333(-3)	3.323(-2)	3.157(-1)	1.409	2.548	1.405	2.541	
40	2.500(-3)	2.494(-2)	2.398(-1)	1.093	2.054	1.091	2.050	
50	2.000(-3)	1.996(-2)	1.934(-1)	8.959(-1)	1.698	8.941(-1)	1.696	
100	1.000(-3)	9.990(-3)	9.832(-2)	4.725(-1)	9.167(-1)	4.721(-1)	9.159(-1)	

Table 2**:** Flow rate phase angle $G_P(\delta,\theta)$ (rad) in terms of gas rarefaction parameter δ and oscillation parameter θ for $H/W=0.1$

δ	$G_P(\delta,\theta)$					$G_P^{(S)}(\delta,\theta)$	
	$\theta=0.1$	$\theta=1$	$\theta=10$	$\theta=50$	$\theta=100$	$\theta=50$	$\theta=100$
0.0001	9.593(-3)	1.179(-3)	1.201(-4)	2.403(-5)	1.201(-5)		
0.001	6.085(-2)	8.113(-3)	8.321(-4)	1.665(-4)	8.324(-5)		
0.01	3.015(-1)	4.828(-2)	5.024(-3)	1.005(-3)	5.026(-4)		
0.05	6.989(-1)	1.487(-1)	1.582(-2)	3.166(-3)	1.583(-3)		
0.1	9.217(-1)	2.343(-1)	2.541(-2)	5.087(-3)	2.544(-3)		
0.5	1.442	6.409(-1)	8.037(-2)	1.612(-2)	8.062(-3)		
1	1.510	9.416(-1)	1.451(-1)	2.924(-2)	1.462(-2)	2.242(-2)	1.121(-2)
2	1.540	1.241	2.901(-1)	5.970(-2)	2.988(-2)	5.191(-2)	2.597(-2)
4	1.555	1.421	6.145(-1)	1.410(-1)	7.085(-2)	1.320(-1)	6.629(-2)
6	1.560	1.473	8.931(-1)	2.481(-1)	1.261(-1)	2.385(-1)	1.210(-1)
8	1.563	1.497	1.082	3.753(-1)	1.949(-1)	3.658(-1)	1.896(-1)
10	1.565	1.512	1.202	5.130(-1)	2.758(-1)	5.044(-1)	2.704(-1)
15	1.567	1.532	1.345	8.340(-1)	5.113(-1)	8.293(-1)	5.067(-1)
20	1.568	1.542	1.405	1.057	7.463(-1)	1.056	7.433(-1)
30	1.569	1.551	1.462	1.274	1.076	1.275	1.075
40	1.569	1.556	1.490	1.360	1.239	1.361	1.240
50	1.570	1.559	1.507	1.405	1.322	1.406	1.322
100	1.570	1.565	1.539	1.492	1.455	1.492	1.455

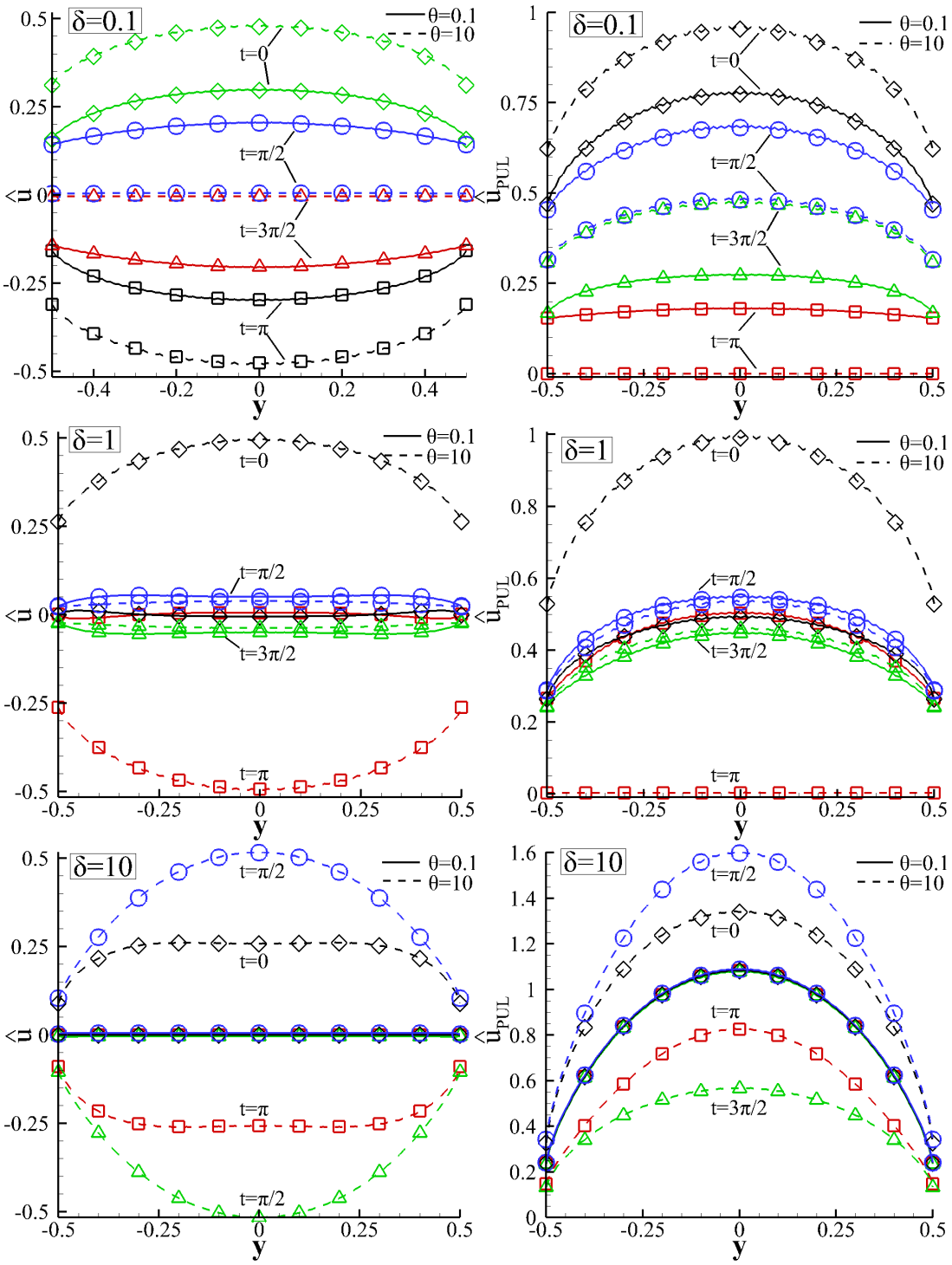

Figure 1: Time evolution of oscillatory $\hat{u}(0,y,t)$ (left) and pulsatile $\hat{u}_{PUL}(0,y,t)$ (right) velocity distributions in terms of distance $y \in [-1/2, 1/2]$ at certain times $t \in [0, 2\pi]$ for $H/W = 1$, $\delta = [0.1, 1, 10]$ and $\theta = [0.1, 10]$.

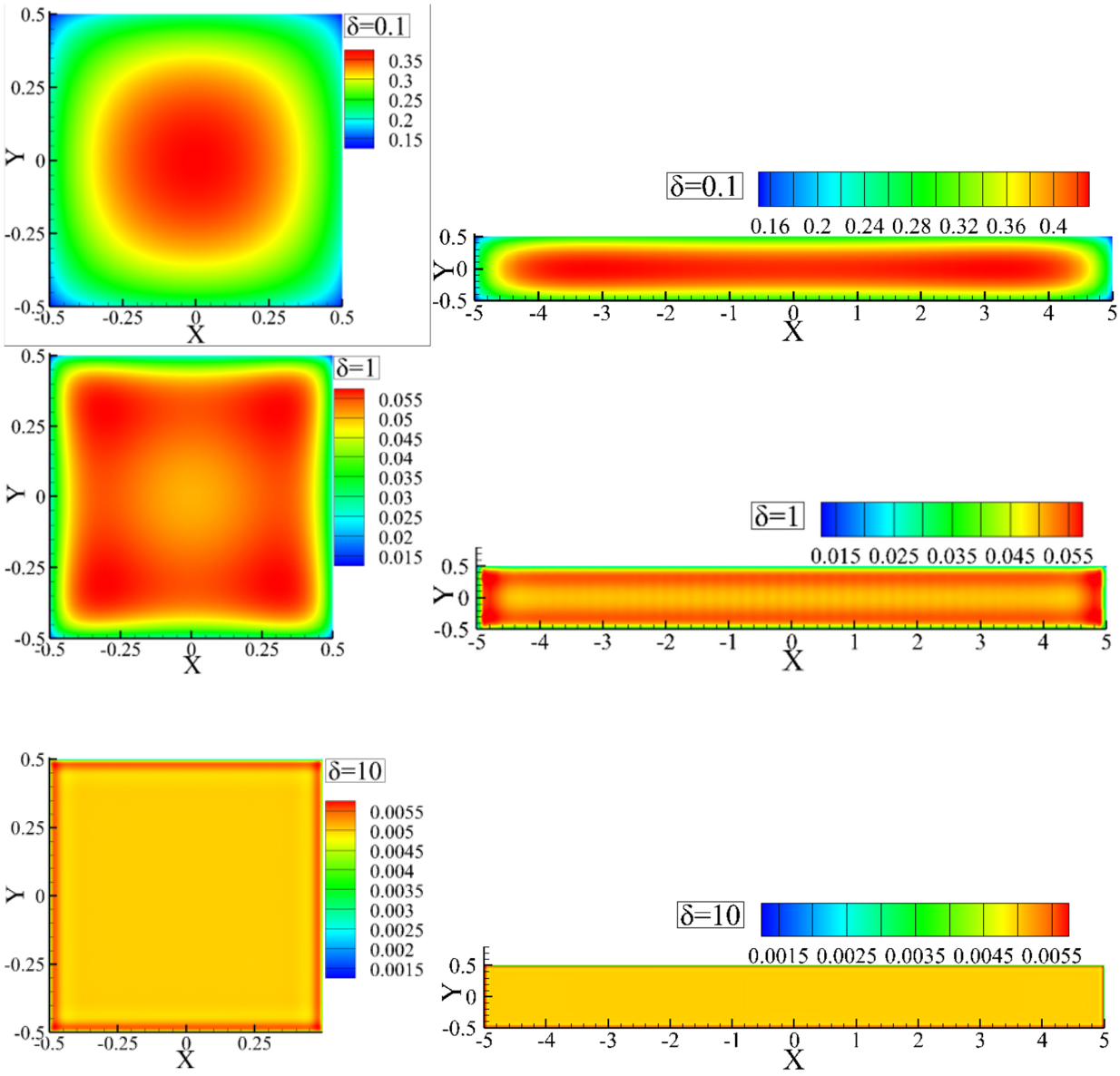

Figure 2**:** Contours of oscillatory velocity amplitude $u_A(x,y)$ for $H/W=1$ (left) and $H/W=0.1$ (right), $\delta=[0.1,1,10]$ and $\theta=0.1$.

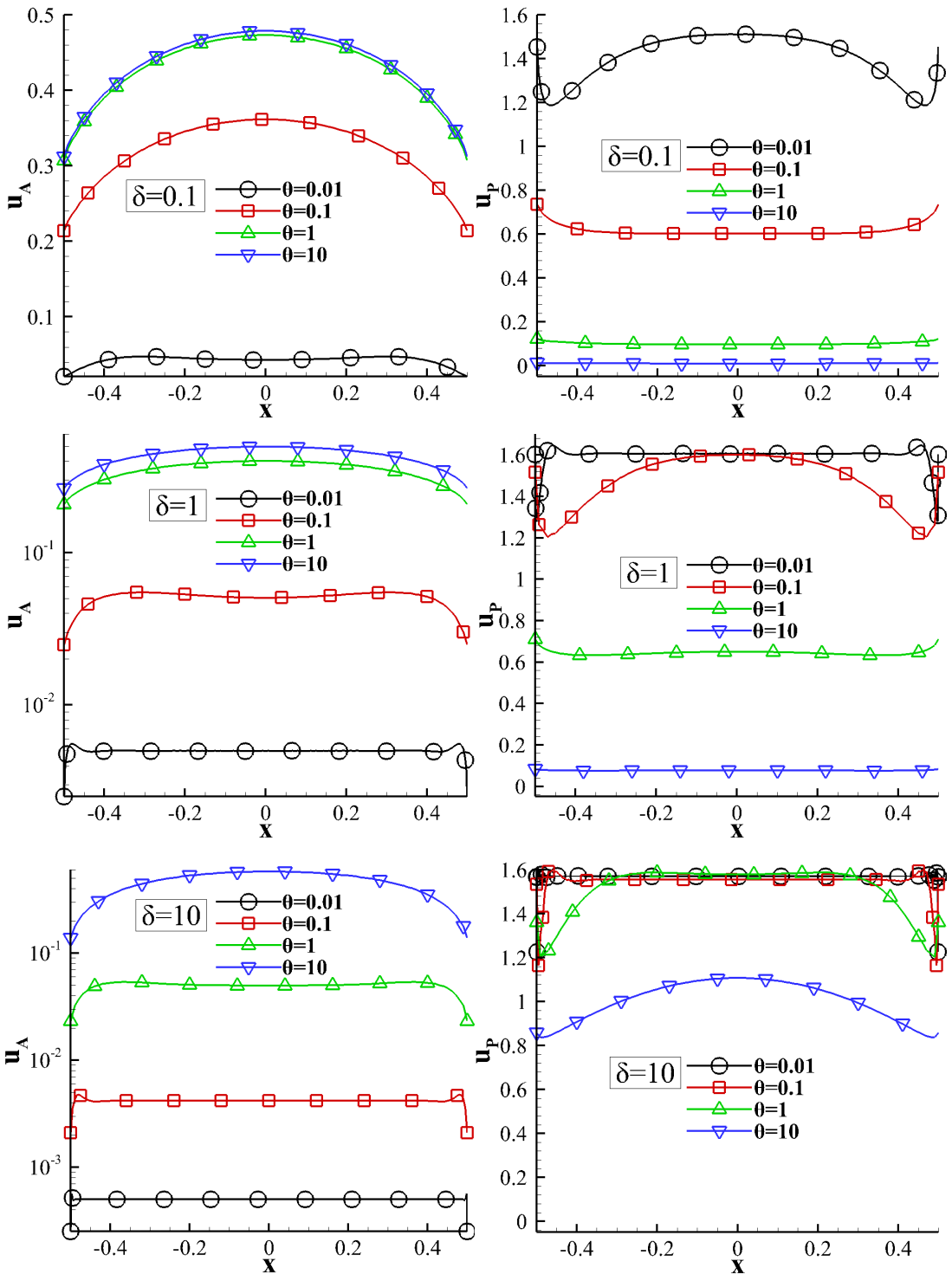

Figure 3: Oscillatory velocity amplitude $u_A(x,0)$ and phase angle $u_P(x,0)$ in terms of distance $x \in [-1/2, 1/2]$ for $H/W = 1$, $\delta = [0.1, 1, 10]$ and $\theta = [10^{-2}, 0.1, 1, 10]$.

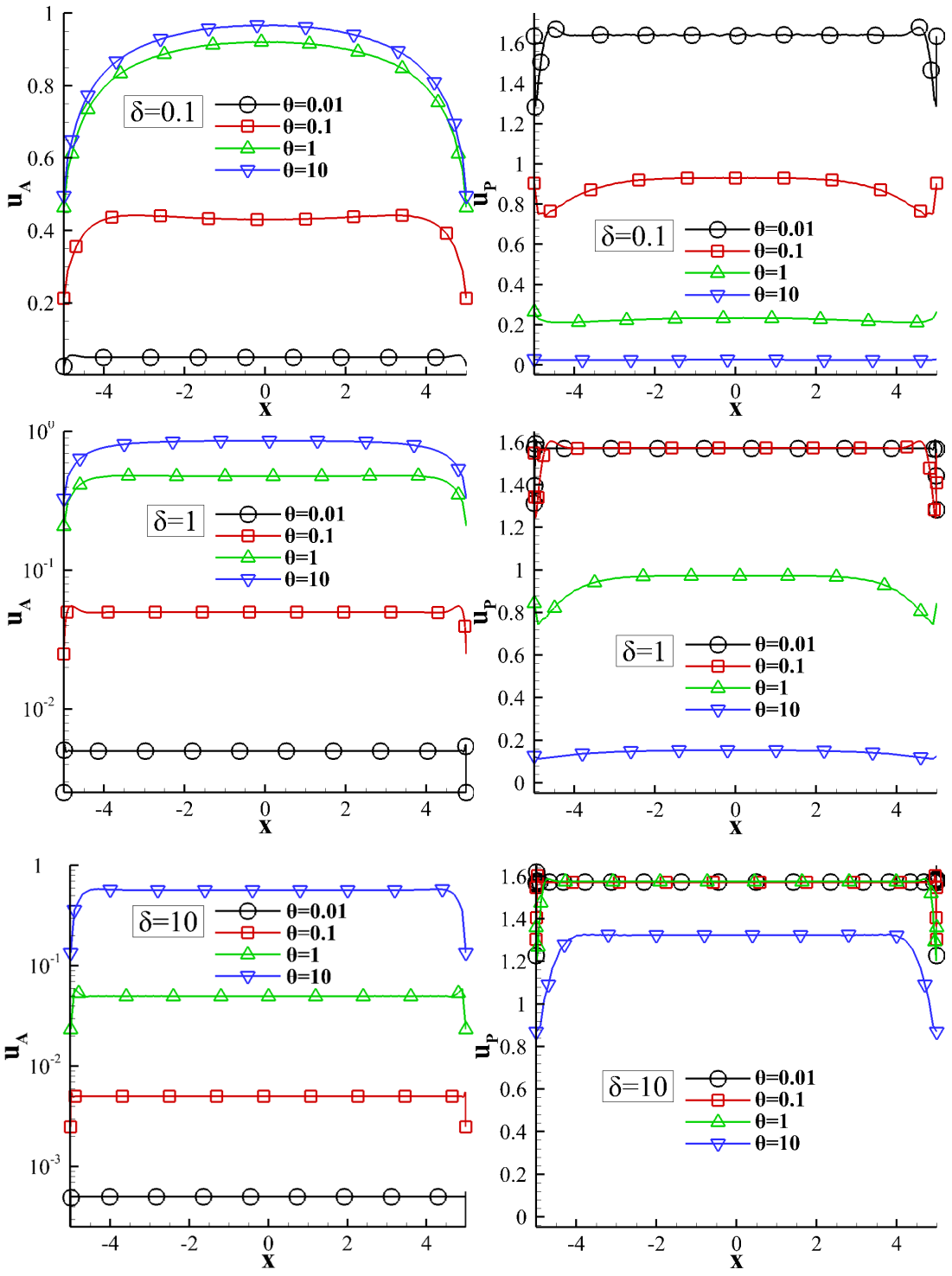

Figure 4: Oscillatory velocity amplitude $u_A(x,0)$ and phase angle $u_P(x,0)$ in terms of distance $x \in [-H/(2W), H/(2W)]$ for $H/W = 0.1$, $\delta = [0.1,1,10]$ and $\theta = [10^{-2}, 0.1,1,10]$.

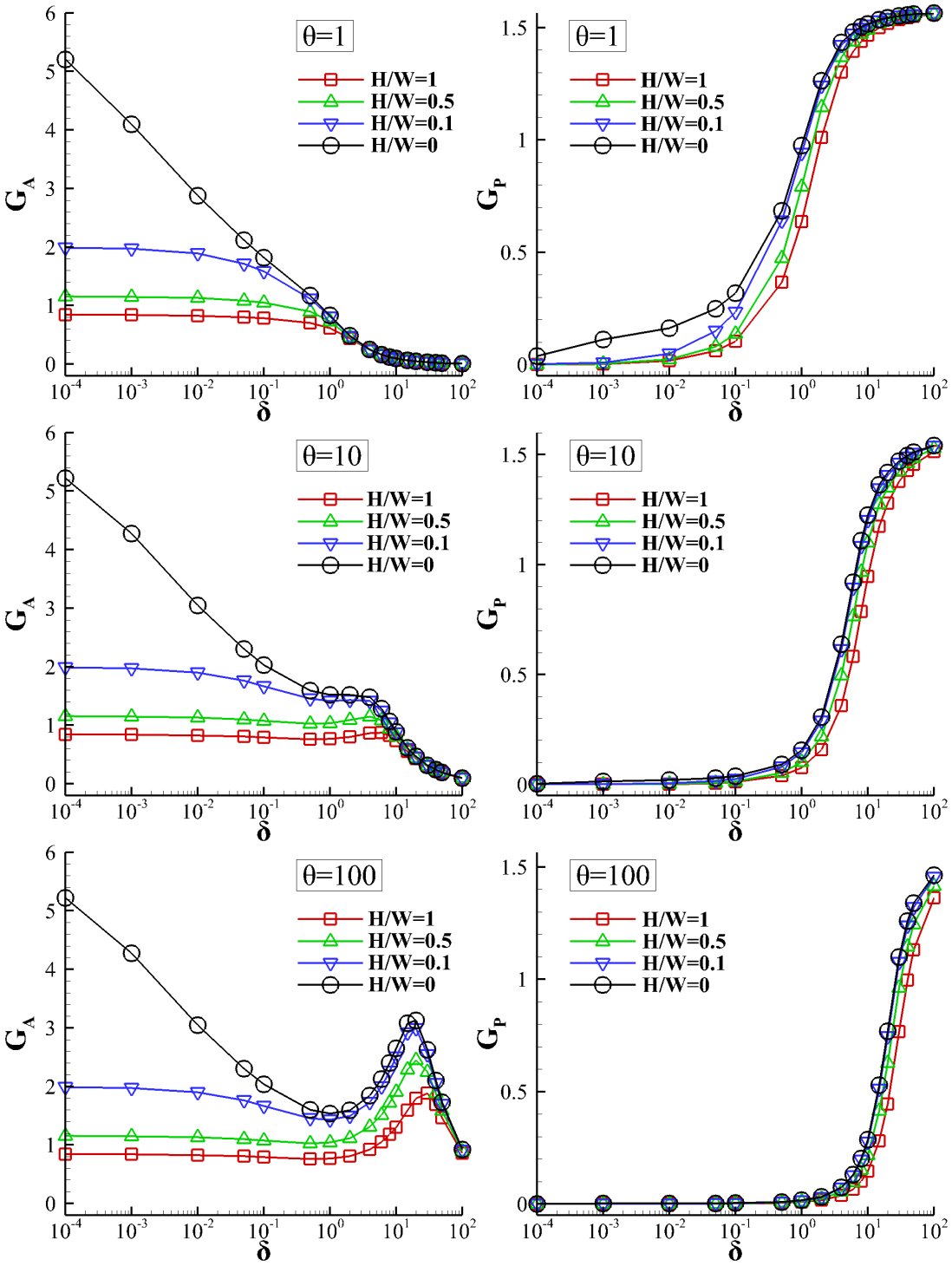

Figure 5: Oscillatory flow rate amplitude G_A and phase angle G_P in terms of gas rarefaction parameter δ for $\theta = \left[1, 10, 10^2\right]$ and $H/W = \left[1, 0.5, 0.1, 0\right]$.

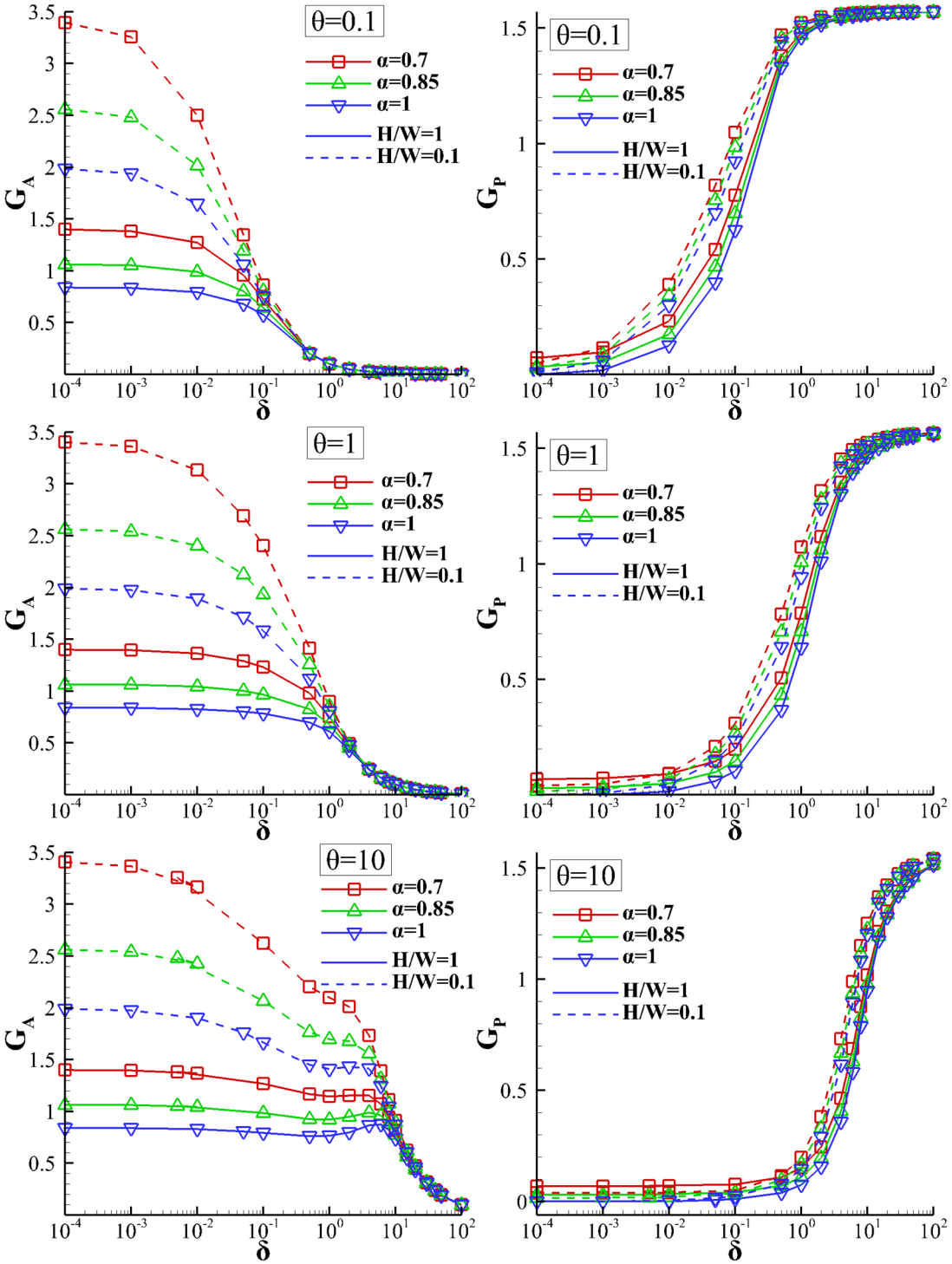

Figure 6: Oscillatory flow rate amplitude G_A and phase angle G_P in terms of the gas rarefaction parameter δ for $H/W=1$ (solid lines) and $H/W=0.1$ (dashed lines), $\theta=\left[10^{-1},1,10\right]$ and accommodation coefficient $\alpha=\left[1,0.85,0.7\right]$.

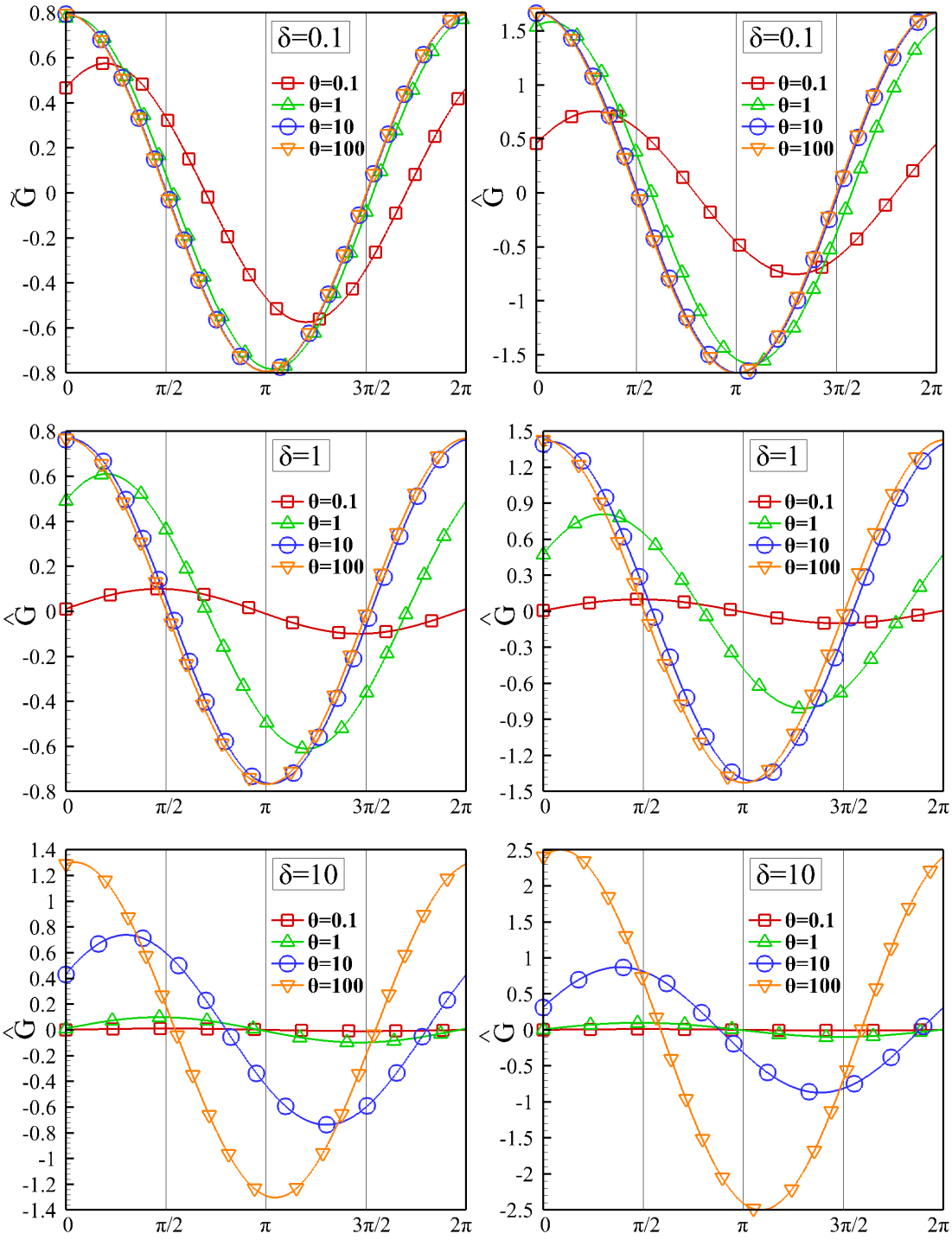

Figure 7: Oscillatory flow rate $\hat{G}$ over one oscillation period for an orthogonal duct with $H/W=1$ (left) and $H/W=0.1$ (right) for $\delta=\left[0.1,1,10\right]$ and $\theta=\left[0.1,1,10,10^2\right]$.

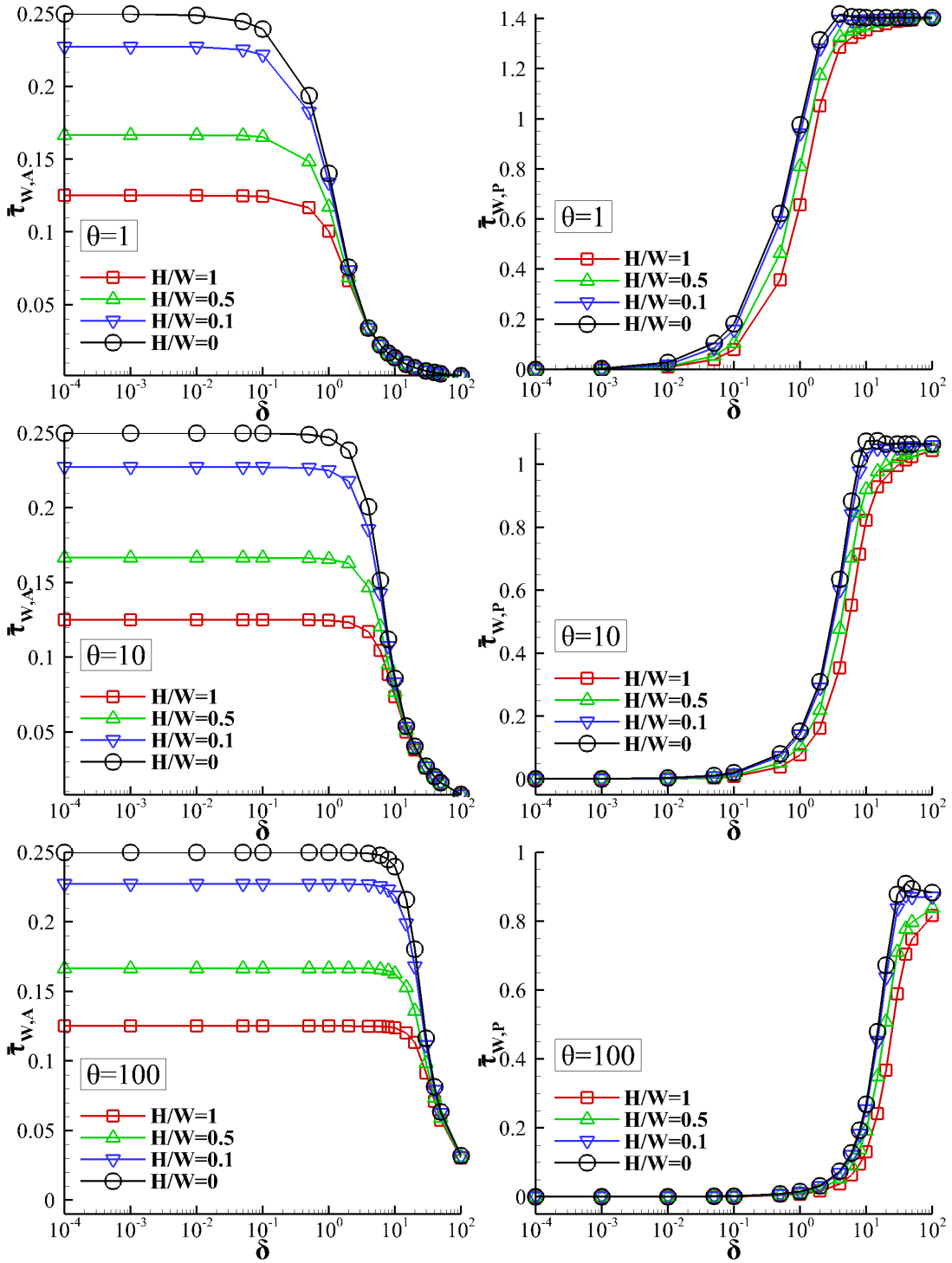

Figure 8: Oscillatory mean wall shear stress amplitude $\overline{\tau}_{W,A}(\delta,\theta)$ and phase angle $\overline{\tau}_{W,P}(\delta,\theta)$ in terms of the gas rarefaction parameter δ for $\theta=\left[1,10,10^2\right]$ and $H/W=\left[1,0.5,0.1,0\right]$..

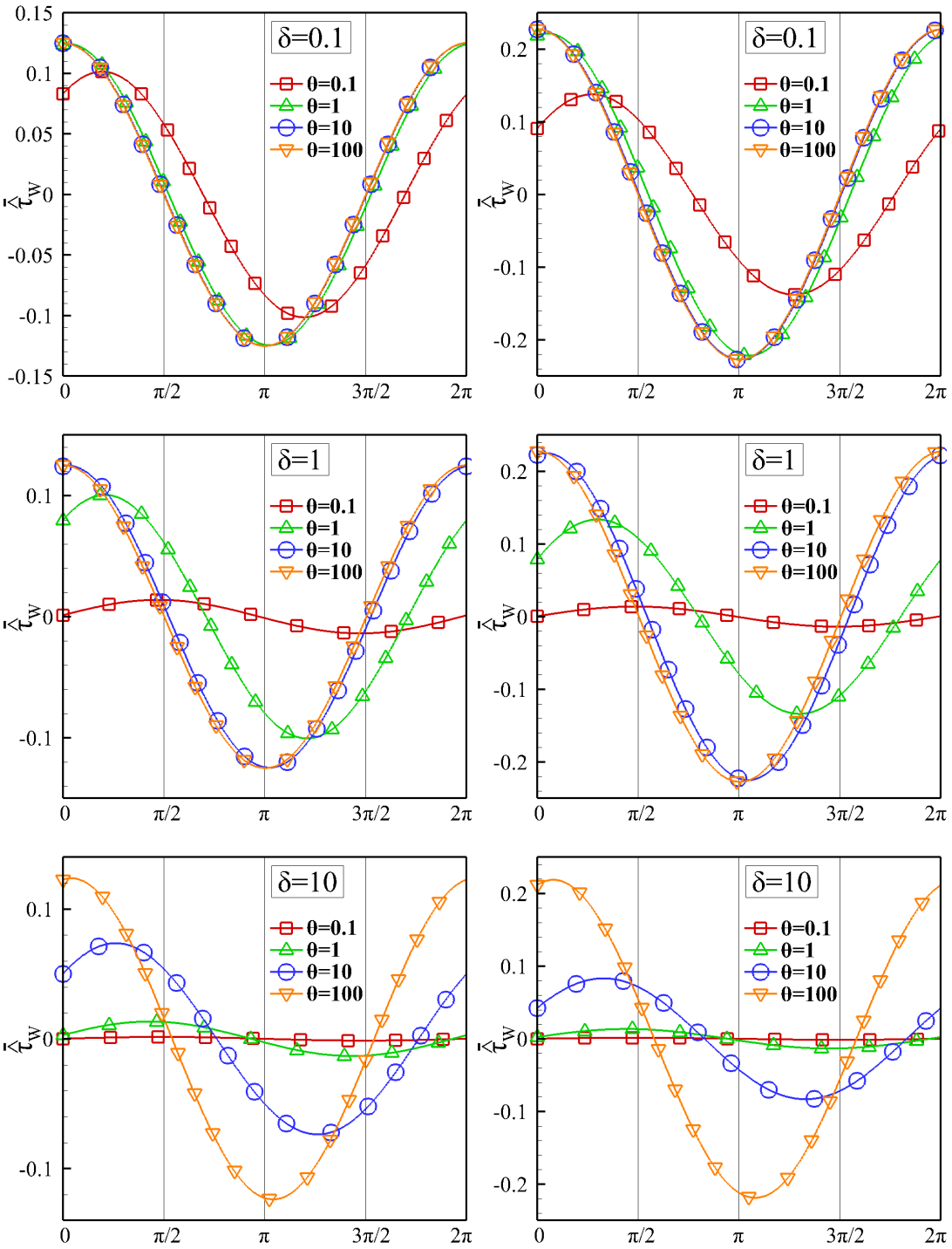

Figure 9: Oscillatory mean wall shear stress $\bar{\hat{\tau}}_W$ over one oscillation period for $H/W=1$ (left) and $H/W=0.1$ (right), $\delta=\left[0.1,1,10\right]$ and $\theta=\left[0.1,1,10,10^2\right]$.

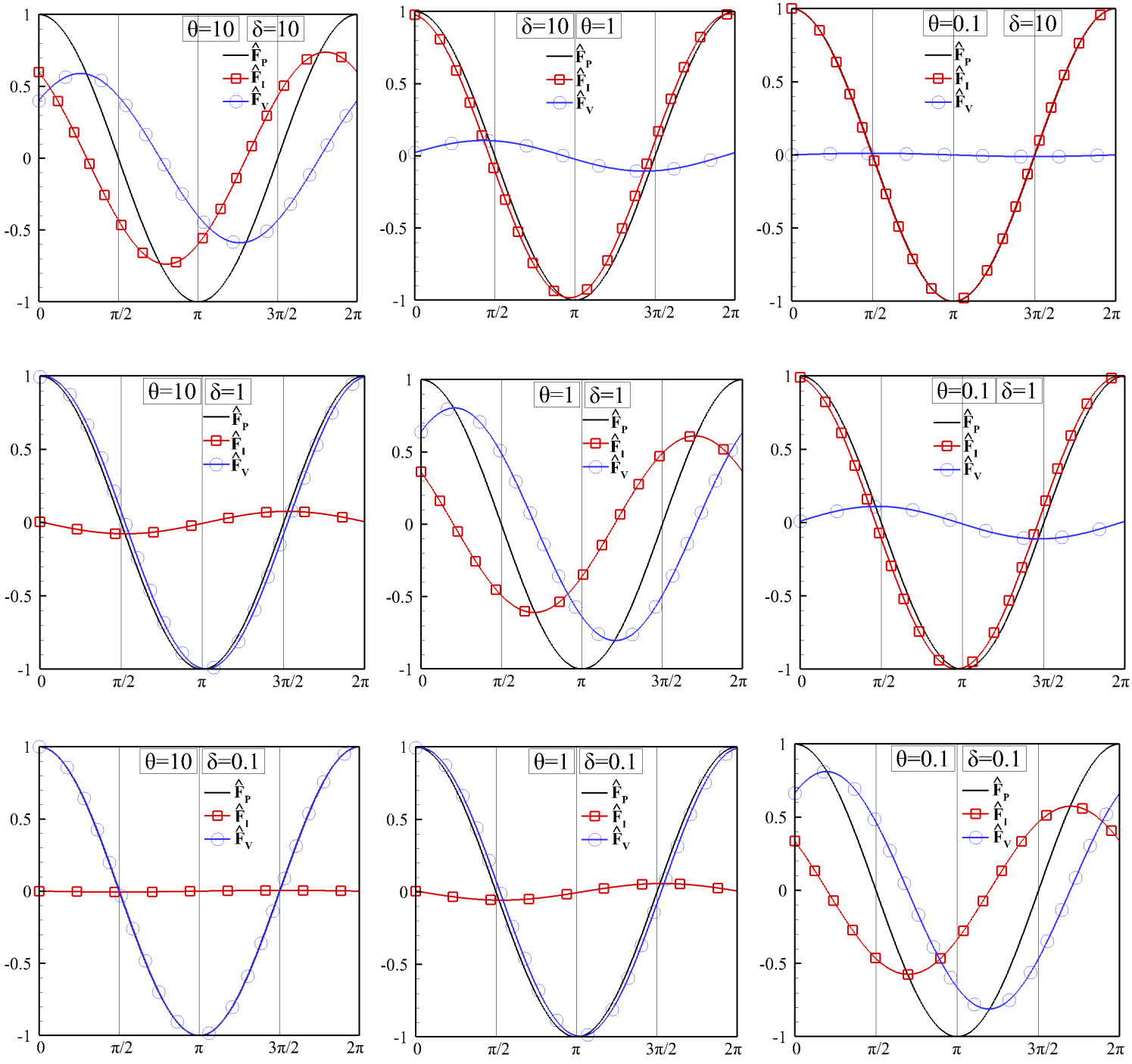

Figure 10: Oscillatory inertia $\hat{F}_I$, viscous $\hat{F}_V$ and pressure $\hat{F}_P$ forces over one oscillation period for $\delta = [0.1,1,10]$, $\theta = [0.1,1,10]$ and $H/W = 1$ (all forces are divided by Adz).

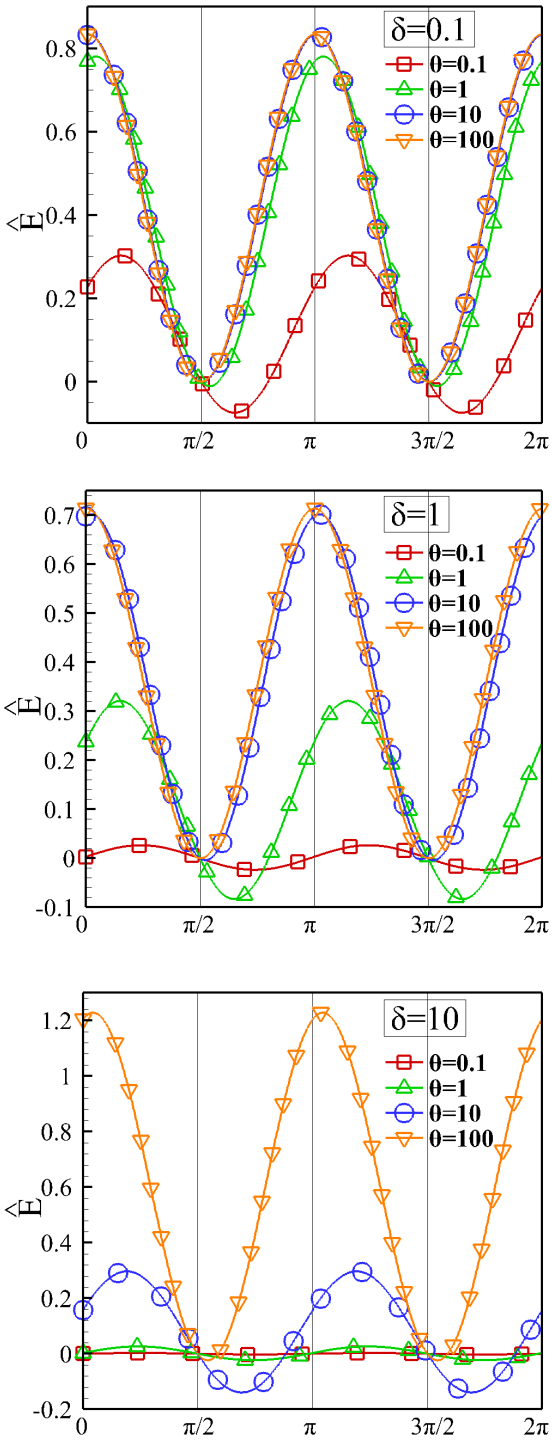

Figure 11: Oscillatory pumping power $\hat{E}$ over one oscillation period for $\delta = [0.1,1,10]$, $\theta = \left[0.1,1,10,10^2\right]$ and $H/W = 0.1$ (pumping power is divided by Adz).

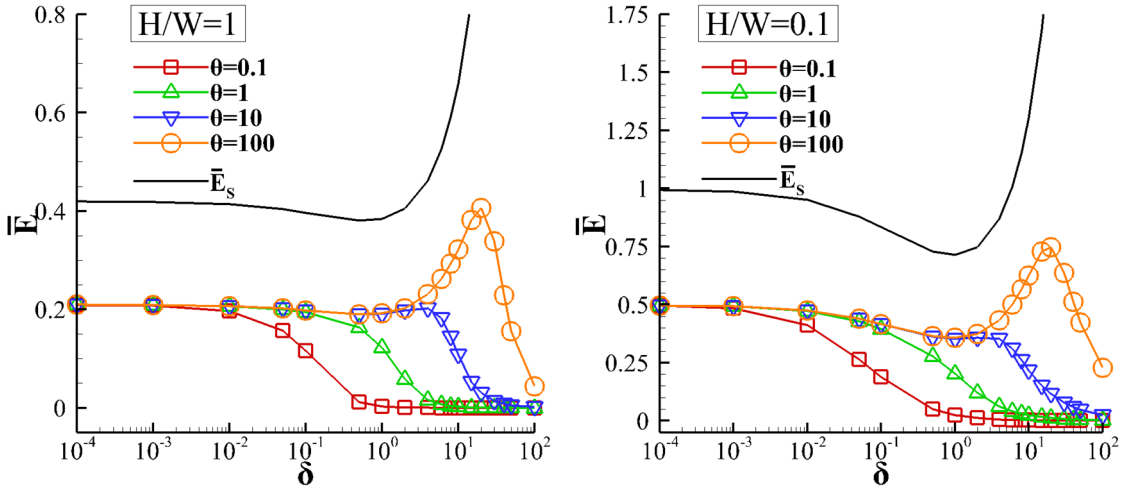

Figure 12: Average pumping power $\bar{E}$ over one period of oscillation along with the steady state pumping power $\bar{E}_S$ in terms of the rarefaction parameter δ for $H/W=1$ (left) and $H/W=0.1$ (right) with $\theta=\left[0.1,1,10,10^2\right]$ (pumping powers are divided by Adz).